



UNIVERSITAT POLITÈCNICA DE CATALUNYA
BARCELONATECH
Escola d'Enginyeria de Barcelona Est

FINAL DEGREE THESIS

Bachelor's Degree in Mechanical Engineering

Bachelor's Degree in Materials Engineering

**DEVELOPMENT OF A VIRTUAL MODEL OF MUSCULOSKELETAL
SOFT TISSUE: APPLICATION TO KNEE MENISCI**



Report

Author: Judit Llop Borràs
Director: Gil Serrancolí Masferrer
Co-director: Lluís Jofre Cruanyes
Department: EM – Mechanical Engineering
Call: June 2023

Abstract

The knee joint, one of the largest and most complex joints in the body, plays a crucial role in supporting locomotion and providing stability to the lower extremities. The synovial cavity and fluid within the knee joint contribute to its overall function by facilitating movement, lubricating the joint, absorbing shock, and supplying nutrients, among others.

This study presents a computational approach using OpenFOAM open-source software to simulate the behaviour of the synovial fluid in one-quarter of the knee cavity. The primary objective of this research is to enhance the geometry representation, achieve a stable simulation and observe the fluid's behaviour within the knee region. Initially, the geometry of the knee cavity is designed and improved in SALOME, an open-source platform for computational fluid dynamics, to represent the anatomical features more accurately. Subsequently, appropriate boundary conditions are defined to simulate the fluid flow within the virtual model through a gait cycle. Through meticulous analysis of the simulation parameters, a stable simulation is achieved. The simulation results are then post-processed using ParaView, an open-source visualization tool. Various analyses are performed, including the extraction of velocity profiles and the assessment of volume variations within the simulated knee cavity.

The obtained results provide valuable insights into the fluid dynamics within the knee cavity, contributing to a deeper understanding of fluid behaviour. The velocity profiles reveal flow patterns and characteristics, while the analysis of volume variations provides information on deformation and fluid redistribution within the knee cavity. The developed virtual model serves as a valuable tool for further research in understanding and analysing the biomechanics of the knee joint and going further with the main project, which aims to develop a multi-scale model that can combine concepts in the field of biomechanics and fluid biodynamics.

Resum

L'articulació del genoll, una de les més grans i complexes del cos, té un paper crucial en la locomoció i l'estabilitat de les extremitats inferiors. La cavitat sinovial i el fluid dins de l'articulació del genoll contribueixen a la seva funció general facilitant el moviment, la lubricació de l'articulació, l'absorció d'impactes i el subministrament de nutrients, entre altres.

Aquest estudi presenta un enfocament computacional utilitzant el programari obert OpenFOAM per simular el comportament del líquid sinovial en una quarta part de la cavitat del genoll. L'objectiu principal d'aquesta investigació és millorar la geometria, aconseguir una simulació estable i observar el comportament del fluid dins de la regió del genoll. Inicialment, la geometria de la cavitat del genoll es dissenya i millora amb SALOME, una plataforma de codi obert per a la dinàmica de fluids computacional, per representar amb més precisió les característiques anatòmiques. Posteriorment, es defineixen les condicions de contorn apropiades per simular el flux del fluid dins del model virtual a través d'un cicle de marxa. Mitjançant una anàlisi meticulosa dels paràmetres de simulació, s'aconsegueix una simulació estable. Els resultats de la simulació es processen posteriorment amb ParaView, una eina de visualització de codi obert. Es realitzen diversos anàlisis, incloent l'extracció de perfils de velocitat i l'avaluació de les variacions de volum dins de la cavitat simulada del genoll.

Els resultats obtinguts proporcionen informació sobre la dinàmica del fluid dins de la cavitat del genoll, contribuint a una comprensió més profunda del comportament del fluid. Els perfils de velocitat revelen els patrons i les característiques del flux, mentre que l'anàlisi de les variacions de volum proporciona informació sobre la deformació i la redistribució del fluid dins de la cavitat del genoll. El model virtual desenvolupat serveix com a eina rellevant per a futures investigacions en la comprensió i l'anàlisi de la biomecànica de l'articulació del genoll, i per continuar amb el projecte principal que té com a objectiu desenvolupar un model multi-escala que pugui combinar conceptes en el camp de la biomecànica i la biodinàmica de fluids.

Resumen

La articulación de la rodilla, una de las más grandes y complejas del cuerpo, desempeña un papel crucial en la locomoción y la estabilidad de las extremidades inferiores. La cavidad sinovial y el fluido dentro de la articulación de la rodilla contribuyen a su función general al facilitar el movimiento, la lubricación de la articulación, la absorción de impactos y el suministro de nutrientes, entre otros.

Este estudio presenta un enfoque computacional utilizando el software abierto OpenFOAM para simular el comportamiento del líquido sinovial en una cuarta parte de la cavidad de la rodilla. El objetivo principal de esta investigación es mejorar la geometría, lograr una simulación estable y observar el comportamiento del fluido dentro de la región de la rodilla. Inicialmente, la geometría de la cavidad de la rodilla se diseña y mejora en SALOME, una plataforma de código abierto para la dinámica de fluidos computacional, para representar con más precisión las características anatómicas. Posteriormente, se definen las condiciones de contorno apropiadas para simular el flujo del fluido dentro del modelo virtual a través de un ciclo de marcha. Mediante un análisis meticuloso de los parámetros de simulación, se consigue una simulación estable. Los resultados de la simulación se procesan posteriormente con ParaView, una herramienta de visualización de código abierto. Se realizan varios análisis, incluida la extracción de perfiles de velocidad y la evaluación de las variaciones de volumen dentro de la cavidad simulada de la rodilla.

Los resultados obtenidos proporcionan información sobre la dinámica del fluido dentro de la cavidad de la rodilla, contribuyendo a una comprensión más profunda del comportamiento del fluido. Los perfiles de velocidad revelan los patrones y las características del flujo, mientras que el análisis de las variaciones de volumen proporciona información sobre la deformación y la redistribución del fluido dentro de la cavidad de la rodilla. El modelo virtual desarrollado sirve como una relevante herramienta para futuras investigaciones en la comprensión y el análisis de la biomecánica de la articulación de la rodilla, y para continuar con el proyecto principal que tiene como objetivo desarrollar un modelo multi-escala que puede combinar conceptos en el campo de la biomecánica y la biodinámica de fluidos.

Acknowledgments

Firstly, I would like to thank my directors of the project, Gil and Lluís, for giving me the opportunity to take part of this ambitious project, for all their support, patience, and kindly help, because they have always been accessible and ready to give some guidance.

I am also immensely grateful for all the help and support I have received from my family and friends, who have always supported and encouraged me throughout my studies and new challenges.

Thanks to you all, today I hand over this project.

Index

ABSTRACT	I
RESUM	II
RESUMEN	III
ACKNOWLEDGMENTS	IV
1. PREFACE	11
1.1. Background	11
1.2. Motivation.....	12
2. INTRODUCTION	13
2.1. Objective	13
2.2. State of the Art.....	14
2.3. Scope of the Project.....	16
3. THEORETICAL FRAMEWORK	18
3.1. Knee Joint Anatomy and Biomechanics	18
3.1.1. Tissues of Knee Joint	19
3.1.2. Synovial Joints	20
3.1.3. Biomechanics of the Knee Joint	20
3.2. Synovial Cavity and Fluid	22
4. METHODOLOGY	24
4.1. Geometry	24
4.1.1. Geometry Improvement.....	24
4.1.2. Geometry Characterisation	26
4.2. Mesh generation.....	27
4.2.1. Mesh Hypothesis.....	27
4.2.2. Sub-meshes Construction.....	28
4.2.3. Patches Creation	30
4.2.4. Mesh Refinement.....	31
4.2.5. Mesh Exportation.....	31
4.3. Movement and Boundary Conditions	32
4.3.1. Boundary Conditions	32
4.3.2. Velocity and Pressure	34
4.3.3. Velocity Calculation.....	37

4.3.4. Simulation Parameter Definition	42
4.4. Solver	45
4.4.1. Navier-Stokes Equations.....	45
4.4.1.1. Mass Conservation	46
4.4.1.2. Momentum Conservation	47
4.4.1.3. Energy Conservation	47
4.4.2. PimpleFoam.....	48
4.5. Post-Processing.....	49
4.5.1. ParaView.....	49
5. RESULTS AND ANALYSIS	50
5.1. Effect of Viscosity on Pressure Results.....	50
5.2. Volume Results	53
5.3. Velocity Results.....	54
5.3.1. Magnitude of Velocity	55
5.3.2. X-direction Velocity (Ux).....	60
5.3.3. Y-direction Velocity (Uy)	66
5.3.4. Velocity Profile	71
5.3.5. Velocity Glyphs.....	73
5.4. Surface Flow.....	76
6. ENVIRONMENTAL ANALYSIS	78
7. CONCLUSIONS	79
ECONOMIC ANALYSIS	81
REFERENCES	82

Index of Figures

Figure 1: Human knee joint [15].	18
Figure 2: Six different types of synovial joints [19].	20
Figure 3: The six degrees of freedom of the TF joint [22].	21
Figure 4: Synovial cavity of the knee joint [24].	22
Figure 5: Lower part of the femur [30].	25
Figure 6: RMI of the knee and the cavity's geometry on top [31].	25
Figure 7: Dimensions of the quarter of the synovial cavity.	26
Figure 8: Resulting improved geometry in SALOME.	27
Figure 9: Resulting quadratic mesh from the improved geometry in SALOME.	29
Figure 10: Resulting mesh with corresponding patches.	30
Figure 11: Unit system in OpenFOAM [33].	37
Figure 12: Velocity values for one cycle of 1s.	38
Figure 13: Eulerian and Lagrangian representation of fluid flow equations [44].	45
Figure 14: Pressure map for nu 1 at 0,36 s.	51
Figure 15: Pressure map for nu 2 at 0,36 s.	51
Figure 16: Pressure map for nu 3 at 0,36 s.	52
Figure 17: Variation of volume during a gait cycle.	53
Figure 18: Geometry with the lines to plot the velocity.	54
Figure 19: Magnitude of velocity at 0.36 s.	55
Figure 20: Coloured map of magnitude of velocity at 0.36 s.	56
Figure 21: Magnitude of velocity at 0.53 s.	56
Figure 22: Coloured map of magnitude of velocity at 0.53 s.	57
Figure 23: Magnitude of velocity at 0.62 s.	57
Figure 24: Coloured map of magnitude of velocity at 0.62 s.	58

Figure 25: Magnitude of velocity at 0.74 s. _____	58
Figure 26: Coloured map of magnitude of velocity at 0.74 s. _____	59
Figure 27: Magnitude of velocity at 0.90 s. _____	59
Figure 28: Coloured map of magnitude of velocity at 0.90 s. _____	60
Figure 29: X-axis velocity at 0.36 s. _____	61
Figure 30: Coloured map of x-axis velocity at 0.36 s. _____	61
Figure 31: X-axis velocity at 0.53 s. _____	62
Figure 32: Coloured map of x-axis velocity at 0.53 s. _____	62
Figure 33: X-axis velocity at 0.62 s. _____	63
Figure 34: Coloured map of x-axis velocity at 0.62 s. _____	63
Figure 35: X-axis velocity at 0.74 s. _____	64
Figure 36: Coloured map of x-axis velocity at 0.74 s. _____	64
Figure 37: X-axis velocity at 0.90 s. _____	65
Figure 38: Coloured map of x-axis velocity at 0.90 s. _____	65
Figure 39: Y-axis velocity at 0.36 s. _____	66
Figure 40: Coloured map of y-axis velocity at 0.36 s. _____	67
Figure 41: Y-axis velocity at 0.53 s. _____	67
Figure 42: Coloured map of y-axis velocity at 0.53 s. _____	68
Figure 43: Y-axis velocity at 0.62 s. _____	68
Figure 44: Coloured map of y-axis velocity at 0.62 s. _____	69
Figure 45: Y-axis velocity at 0.74 s. _____	69
Figure 46: Coloured map of y-axis velocity at 0.74 s. _____	70
Figure 47: Y-axis velocity at 0.90 s. _____	70
Figure 48: Coloured map of y-axis velocity at 0.90 s. _____	71
Figure 49: Velocity profile for $x=2.7$ cm at different time steps. _____	72
Figure 50: Velocity glyphs at 0.36 s. _____	73

Figure 51: Velocity glyphs at 0.37 s. _____	73
Figure 52: Velocity glyphs at 0.38 s. _____	73
Figure 53: Velocity glyphs at 0.39 s. _____	73
Figure 54: Velocity glyphs at 0.45 s. _____	74
Figure 55: Velocity glyphs at 0.52 s. _____	74
Figure 56: X-direction velocity glyphs at 0.52 s. _____	74
Figure 57: Y-direction velocity glyphs at 0.52 s. _____	74
Figure 58: Velocity glyphs at 0.53 s. _____	75
Figure 59: Velocity glyphs at 0.54 s. _____	75
Figure 60: Velocity glyphs at 0.55 s. _____	75
Figure 61: Extract Block filter in movingWall boundary in ParaView. _____	76
Figure 62: Capture of surface flow in ParaView. _____	77
Figure 63: Greenhouse gas emissions (GHG) of an HP Envy 16inch laptop. _____	78

1. Preface

This project serves as the final project for a student pursuing a double bachelor's degree in Mechanical Engineering and Materials Engineering. During the study, competencies from both fields have been extensively used, often making it challenging to distinguish between the two. In the initial sections of the thesis, no explicit differentiation will be made between the two areas, as a comprehensive understanding of the subject matter requires integration of knowledge from both disciplines. Consequently, the introduction, theoretical framework, and methodology sections will be shared, emphasizing the interdisciplinary nature of the research.

However, in the subsequent chapter dedicated to results and analysis, a distinction will be made between the contributions from each discipline. Within the context of the Mechanical Engineering degree, the analysis of velocity profiles will be emphasized, focusing on understanding the fluid dynamics within the knee joint. On the other hand, within the framework of the Materials Engineering degree, the analysis will be centred around different viscosities, investigating the impact of varying fluid properties on the behaviour of the synovial fluid.

This differentiation in the results and analysis chapter allows for a comprehensive exploration of the research objectives from both disciplinary perspectives. By delving into the specific aspects relevant to each field, a better understanding of the fluid dynamics in the knee joint can be achieved, integrating the knowledge and insights derived from both disciplines.

1.1. Background

This study represents a bachelor's thesis that builds upon previous studies carried out by previous students in recent years. This study takes part in a large-scale project that seeks to develop a multi-scale model capable of integrating concepts in the field of biomechanics and fluid dynamics. The project objective is to bridge the gap between different software that combine both disciplines, biomechanics, and fluid dynamics.

In the previous studies, a brief introduction to the software has been provided and the synovial cavity of the knee has been modelled. The following studies have incorporated more precise properties for the synovial fluid and the cavity. The present study aims to improve the geometry of the synovial cavity as well as the boundary conditions to achieve a better approximation of reality.

1.2. Motivation

The main motivation for carrying out this work is its connection to simulation and engineering. I developed a strong interest in various subjects during my studies and among them are fluid engineering and finite element methods simulation. Although I have enjoyed studying these topics, I have only been able to work with mechanical simulation and not fluid simulation. Therefore, this study was an opportunity for me to challenge myself and explore a new facet of simulation, named computational fluid dynamics, and its various applications. Moreover, the fact that this project is related to the health sciences excites me and motivates me to put forth my best effort. The idea that my little contribution to the project could aid in medical research and potentially enhance someone's quality of life is inspiring. I am committed to working with purpose, and in my opinion, there is no better way to apply engineering than by working towards a better society and having a positive impact on others.

Right from the start, I knew this project would be a significant challenge for me since it involves learning how to use software from scratch. I needed to enhance my coding abilities and be prepared to spend long hours on the computer, potentially without any immediate results. However, I realized this would be a valuable opportunity for me to learn and enjoy, and that's precisely what has happened.

2. Introduction

The musculoskeletal system plays a vital role in enabling the human body to carry out daily activities, from simple movements like walking to more complex activities such as athletics or running. To better understand the biomechanics of the knee menisci, researchers have turned to computational models, using simulation software to develop virtual models. The resulting model can be used to simulate various movement scenarios, along with stress and strain analysis of the soft tissue therefore, computational models have become increasingly important in many scientific fields, including biomechanics. Nevertheless, these models come with some challenges, such as the validation of the model, it can be difficult or almost impossible to validate it, as sometimes experimental data for comparison cannot be obtained.

This study builds upon previous studies in which a quarter of the knee synovial cavity was modelled using the OpenFOAM software. The initial study was the first approach with OpenFOAM, including a brief introduction to the software. The synovial cavity was designed and later, a random vertical movement was added to obtain a dynamic mesh. Although a stable model was obtained, limitations in the accuracy of properties and dimensions precluded meaningful conclusions. In the subsequent study, physical characteristics and properties of the synovial fluid and cavity were introduced in the model, along with a realistic movement representing the movement of the femur when an individual is walking.

Following the path of these previous studies, in this present study, the design of the synovial cavity geometry will be improved to have a more realistic approach. Boundary conditions of the simulations will be also modified to follow the approach of simulating one-quarter of the cavity, saying that the cavity is symmetric. Once an accurate and refined mesh is obtained and the simulation is stable, the analysis of the fluid movement, volume and velocities will be performed.

2.1. Objective

The final objective of this large-scale project is to develop a multi-scale analysis model able to combine Open Sim [1], a biomechanics software designed for multi-solid systems, and OpenFOAM [2], a fluid dynamics software. This present project aims to develop a virtual model of musculoskeletal soft tissue, with a focus on the knee menisci, using OpenFOAM simulation software. The specific objective of this study is to improve and develop further the knee synovial cavity's geometry, establish a stable dynamic mesh, and adjust the boundary conditions to get an accurate simulation of the movement approximated to a human gait cycle.

2.2. State of the Art

Computational Fluid Dynamics (CFD) simulations have been used extensively to study the fluid dynamics in the knee joint, which is a complex biomechanical system. In recent years, there have been significant advancements in knee modelling techniques and the accuracy of CFD simulations. However, a limitation in most of the studies is that they do not consider the cartilage and meniscus as biphasic material, as it has both solid and fluid phase or that they do not simulate the synovial fluid inside the cavity nor in a geometry similar to the cavity. Here are some surveys and review papers that study the modelling of synovial fluid in the knee joint:

1. "Mathematical Modelling of Synovial Fluids Flow" by P. Pustejovská [3]. This study models the synovial fluid flow, describing the fluid as an incompressible, viscous and non-Newtonian fluid, inside a two-dimensional rectangular domain with a focus on biochemical and rheological properties of the synovial fluid. The researcher propose two different viscosity models, which are derived from a combination of experimental data and numerical solutions. In contrast to the current study, the main difference lies in the fluid type being considered. While this study treats the synovial fluid as a non-Newtonian fluid, the current study investigates a Newtonian fluid. However, both studies share the common characteristics of incompressibility and being modelled within a two-dimensional cavity. It is important to note that the non-rectangular approach adopted by the current study is more appropriate for accurately representing the synovial knee cavity, unlike the rectangular approach used in this study.
2. "Computational Model for the Generalised Dispersion of Synovial Fluid" by M. Alshehri and S. K. Sharma [4]. In this study the theory of the convective diffusion mechanism occurring in the knee is studied, using a configuration of bearing model for analysis of two rectangular plates of infinite length. The partial differential equations are solved for the Newtonian fluid and an analytical solution for the unsteady dispersion problem has been obtained, which allows to understand better the nutritional transport phenomena of the synovial joint. The synovial fluid is represented as a viscous Newtonian fluid located between two rigid plane surfaces that are approaching each other. To represent the cartilage, a porous boundary is taken into account. While the study primarily focuses on the knee cavity bearing rather than fluid motion, a two-dimensional rectangular plate is used as the domain, which is reasonable but not ideal since it does not simulate the actual geometry of the synovial cavity. The key finding of the study is the distribution of nutrients through the synovial fluid, which is influenced by the concentration of hyaluronic acid molecules and other proteins, using a mathematical model.

3. “A Model of Synovial Fluid Lubricant Composition in Normal and Injured Joints” by M. Blewis, G. Nugent-Derfus, T. Schmidt, B. Schumacher, and R. Sah [5]. The objective of this study was to create a quantitative intercompartmental model that could predict the concentration of synovial fluid lubricants in the knee joint. The model consists of a synovial fluid compartment surrounded by articular cartilage and a semi-permeable synovial membrane, and was designed to integrate various biophysical processes, enabling the identification of environmental and clinical factors that impact the composition of synovial fluid. An advantageous aspect of this study was the integration of multiple layers, including the inclusion of cartilage and the synovial membrane. While this approach is commendable, it is important to note that the model primarily focused on biological aspects.
4. “Computed Synovial Fluid Flow in a Simple Knee Joint Model” by K. Pekkan, R. Nalim and H. Yokota [6]. The study focuses on predicting shear stress induced by fluid flow on knee joint cells, represented in a sinusoidal oscillating flat plate. It examines oscillatory flow of a Newtonian synovial fluid in two-dimensional joint geometries using an experimental model. Additionally, the effect of articular cartilage curvature is investigated in a model with and without menisci. Like the current study, the synovial fluid is considered Newtonian and the domain in this research is also two-dimensional. A notable aspect is the investigation of fluid motion within curved cartilage, and investigating how the inclusion of the menisci in the model affects the shear stresses. On the other hand, a sinusoidal oscillating flat plate typically represents a simplified mechanical system but comparing a knee synovial cavity to it may not be the most appropriate approach. While both involve oscillatory motion, the nature and behaviour of a knee synovial cavity and a sinusoidal flat plate are fundamentally different, a knee synovial cavity is a complex structure with fluid-filled compartments, cartilage, and other anatomical features.
5. “Numerical Modeling of the Knee Synovial Joint Under Deformation Using the Finite Volume Method” by N. Martínez-Gutiérrez, L. A. Ibarra-Bracamontes, S. R. Galván-González, A. Aguilar-Corona & G. Viramontes-Gamboa [7]. In this study, a two-dimensional model of a knee synovial joint is presented, focusing on the angular pressure distribution along the synovial fluid-cartilage interface under simulated loads. The model incorporates a mobile circular wall for the condyle, a larger circular wall for the condylar concave cavity, porous medium for the articular cartilage, and high viscosity Newtonian fluid for the synovial fluid. This study incorporates the loads experienced by the knee, which is expected to yield favourable outcomes. It also includes an analysis of the interaction between the fluid and cartilage at the interface, while defining the synovial fluid as Newtonian, akin to the current study. Although this study may seem the most advanced and bears similarities with the current study, primarily

focuses on pressure rather than fluid motion and utilizes a quarter-circle geometry as an approximation, the geometry should aim for greater accuracy. A positive aspect of this study is the consideration of porous cartilage in the analysis of angular pressure distribution and the inclusion of compressive movement in the model. However, the study does not further investigate fluid motion.

6. “On the Modelling of Synovial Fluid” by J. Hron, J. Málek, P. Pustějovská, and K. Rajagopal [8]. In this study, researchers focused on synovial fluid, describing it as a polymeric liquid with viscoelastic properties due to the presence of hyaluronan (HA) molecules. Depending on the concentration of HA the synovial fluid was having a Newtonian or non-Newtonian behaviour. The authors examined the behaviour of synovial fluid when it behaves as a viscous fluid. They developed a new generalized power-law fluid model that incorporates the concentration of hyaluronan as a factor in determining the power-law exponent. The researchers aimed to describe the flow of synovial fluid inside a rectangular cavity under certain conditions, assuming that it is not subjected to immediate changes. The model included constraints of incompressibility, the balance of linear momentum, and a convection-diffusion equation to account for the concentration of hyaluronan. To validate their models, the researchers compared their results with predictions from a previously used model for synovial fluid. One model had a very good approach to studying the fluid behaviour, but in the end, the simulation was not conducted inside a real-shaped cavity but rather a rectangular one.

2.3. Scope of the Project

This study is part of an ongoing project aimed at developing a virtual model that accurately replicates the knee. The global objective of this project is to provide a dynamic virtual representation of the knee allowing for monitoring, analysis, and optimization. This actual study builds upon previous final degree [9] or master projects [10], using and refining existing data while also incorporating additional improvements to enhance accuracy.

In previous studies, an introduction to OpenFOAM software was conducted, which provided beneficial in gaining familiarity with the software before embarking on the actual project. Additionally, a preliminary simulation approach from the quarter of the synovial cavity of the knee was obtained from previous studies, which helped understanding how to address the problem of study. In those previous studies, a first geometry was designed and a simulation with a vertical movement was performed. Building upon this foundation and once acquainted with the software, the next step involved an

improvement of the synovial cavity geometry to attain a more accurate representation, ensuring at the same time a stable dynamic mesh and readjusting the boundary conditions for accurate simulation.

The primary limitation of the project is the time allocated for a Bachelor thesis, in this case a double Bachelor thesis. While there may be a desire to investigate deeper into the subject matter, it is crucial to adapt the research to accommodate the time constraint.

3. Theoretical Framework

3.1. Knee Joint Anatomy and Biomechanics

The knee joint is essentially made up of three bones: the thigh bone (femur), the shinbone (tibia) and the kneecap (patella). The joint head of the femur has two strong bony projections, the condyles, which are covered with articular cartilage. The articular surface of the tibia is called the tibia plateau [11].

The human knee is the largest joint in the musculoskeletal system, which supports the body weight and facilitates locomotion. The knee consists of two distinct articulations, the tibiofemoral and the patellofemoral joints [12]. The tibiofemoral joint is one of the most complex articulations of the human body and its main tissues are the femur, tibia, fibula, articular cartilages, menisci, and ligaments. The tibiofemoral joint enables the relative motion of the femur and tibia, which is facilitated through mechanical contacts between the cartilages and menisci [13]. Another articulation is the patellofemoral. The function of the patella is multifaceted. Its primary purpose is to serve as a mechanical pulley for the quadriceps as the patella changes the direction of the extension force throughout knee range of motion [14]. A human knee joint can be seen in Figure 1.

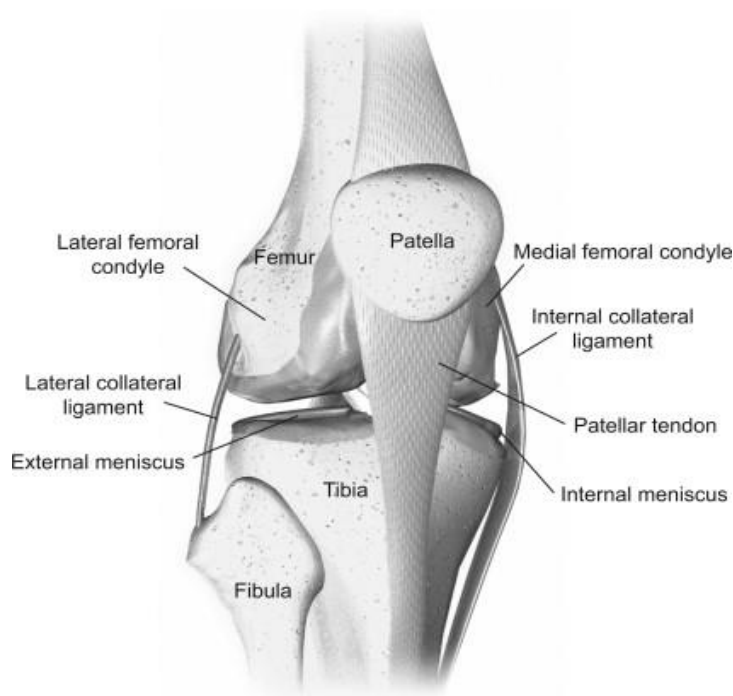


Figure 1: Human knee joint [15].

3.1.1. Tissues of Knee Joint

In the Knee Joint apart from the hard tissues, the bones described above, soft tissues can be found. There are different types of soft tissue:

- Cartilage: slippery and flexible, hyaline (articular) cartilage within the knee joint allows, has less friction than two pieces of glass placed together. This allows the joint to move with minimal friction in a healthy knee. There are two primary types of cartilage in the knee: Articular (Hyaline), which covers the bones where they meet at the knee joint, and Meniscus (Fibrocartilage), two C-shaped cartilaginous structures within the knee [16].
- Tendons: are flexible tissues that attached muscle to bone. In the knee 3 different can be found:
 - o The hamstring, there are three hamstring tendons that cross the knee joint on the back of the knee. Two are on the inside (medial) part of the knee attaching to the shin bone (Semimembranosus and Semitendinosus) and one is on the outside (lateral) part of the knee, attaching to the fibula (Biceps femoris).
 - o The quadriceps, this tendon is composed of contributions from the four quadriceps muscles (the vastus lateralis, vastus intermedius, vastus medialis, and rectus femoris). It attaches the powerful quadriceps muscles to the top part of the patella.
 - o The patellar, which attaches the bottom part of the patella to the top part of the tibia.
- Ligaments: fibrous bands of tissue that connect bones to other bones. In the knee 4 can be found:
 - o the Anterior Cruciate Ligament (ACL), that connects the tibia to the femur and functions to prevent the tibia from sliding forward on the femur.
 - o The Posterior Cruciate Ligament (PCL). The PCL also connects the tibia to the femur. It functions to prevent the tibia from sliding backward on the femur. The PCL works with the ACL for stabilization of the knee.
 - o The Lateral Collateral Ligament (LCL). The LCL, which is also known as the fibular collateral ligament, is located on the outside (lateral side) of the knee. It connects the outside, bottom edge of the femur to the outside, top edge of the fibula. The LCL helps stabilize the knee joint by limiting outward (varus) force across the knee.
 - o The Medial Collateral Ligament (MCL). The MCL is located on the inside (medial side) of the knee, connecting the inside, bottom edge of the femur with the inside, top edge of the tibia. The MCL helps to stabilize the knee by limiting inward (valgus) force across the knee. The MCL works with the LCL to prevent unwanted side-to-side motion.
- Membrane: the synovial membrane surrounds all the joints in the knee and holds the synovial fluid inside. This fluid will provide lubrication and necessary nutrients to the knee joint [16].

3.1.2. Synovial Joints

The classification of joints is based on the amount of movement possible. All diarthroses, or freely movable joints, are synovial joints because they share similarities of structure [17]. Because of the presence of a synovial membrane, diarthrodial joints are often referred to as synovial joints [18]. Seven different categories of diarthrodial (synovial) joints exist, each with unique functional abilities; however, all synovial joints contain the seven common elements: synovial fluid, articular cartilage, articular capsule, synovial membrane, capsular ligaments, blood vessels and sensory nerves[17]. In Figure 2, six different types of synovial joints are shown, being A: Plane, B: Hinge, C: Pivot, D: Ball-and-socket, E: Condyloid and F: Saddle type.

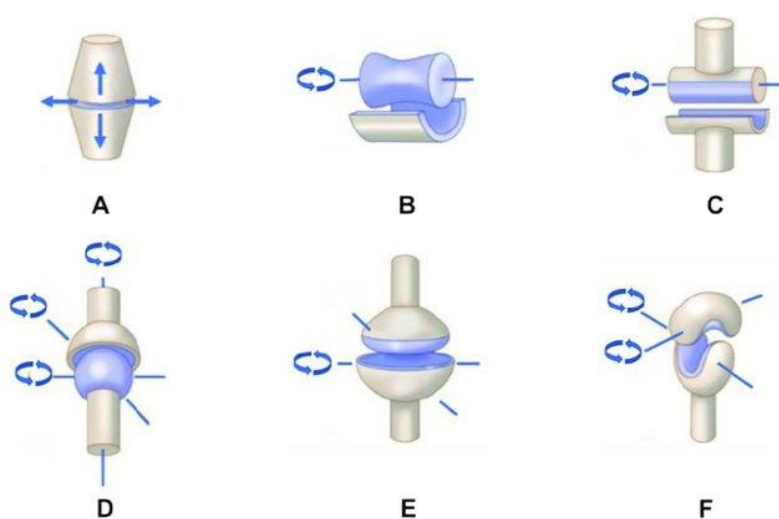


Figure 2: Six different types of synovial joints [19].

In the case of study, the knee joint, it is a bi-condylar type of synovial joint, which mainly allows for flexion and extension (and a small degree of medial and lateral rotation). Condyloid joints are composed of the articulation between a large, rounded, convex member and a relatively shallow concave member. Most often, these joints allow 2 degrees of freedom; ligaments as well as the bony structure of the joint typically prevent motion from occurring in a third plane [17].

3.1.3. Biomechanics of the Knee Joint

The knee joint comprises two distinctly separate joints/articulations; the tibiofemoral (TF) joint - the articulation of the femur over the tibia - and the patellofemoral (PF) joint - the articulation of the patella over the femur. The main roles of the knee joint complex are to allow locomotion with minimum energy requirements from the muscles and stability, accommodating for different terrains; and to

transmit, absorb and redistribute forces caused during the activities of daily life[20]. The movement of the knee joint involves several key actions, primarily flexion and extension, but also including slight rotation and gliding movements.

The primary motion of the TF joint is rotation in the sagittal plane (flexion-extension); therefore, a simplified description is that it acts as a hinge joint in the sagittal plane. The complex three-dimensional motion of the TF joint can be described through six degrees of freedom (three rotations and three translations [21]. The six degrees of freedom of TF joint motion are visible in Figure 3. Mediolateral and flexion-extension movements take place along the epicondylar femoral axis, while joint distraction and internal-external rotation occur along the tibial long axis. Anterior-posterior translation and varus-valgus rotation occur along a floating axis that is perpendicular to both the femoral epicondylar and tibial long axes.

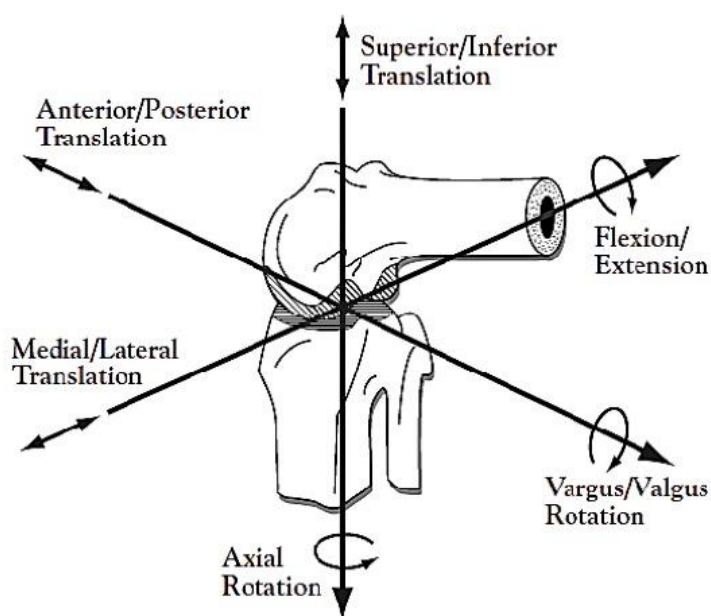


Figure 3: The six degrees of freedom of the TF joint [22].

At full extension, usually defined when the long axes of the tibia and femur are aligned in the sagittal plane, the femur is internally rotated with respect to the tibia and is located anterior to the mid-point of the tibial plateau [20], [21]. As the knee flexes, the lateral condyle of the femur consistently translates posteriorly on the lateral tibial plateau with increasing flexion. Active knee flexion is possible primarily through hamstring contraction and usually reaches 130°, whereas passive flexion can reach 160° [21]. The medial condyle on the other hand experiences a less consistent motion pattern that includes posterior translation and anterior slide during knee flexion. This leads to a reduced overall posterior translation of the medial condyle on the medial tibial plateau from full extension to maximum knee flexion. The larger magnitude of the lateral femoral translation, when coupled with a lesser

translation of the medial femoral translation, leads to the femur externally rotating with respect to the tibia as the knee flexes [20].

This complex mechanism of knee joint motion means that the geometry itself is not adequate to maintain stability, requiring input from passive soft tissue (e.g., ligaments) and muscle tensions. It also means that large forces acting on small articulating areas generate high articular stresses, commonly called joint contact pressure [21].

3.2. Synovial Cavity and Fluid

The synovial cavity of the knee, also known as the knee joint cavity, is a space within the knee joint that is filled with synovial fluid, a representation is shown in Figure 4. The purpose of this fluid is to lubricate the cartilage of the bone joint and provide nourishment through diffusion. It is made from an ultrafiltrate of blood plasma and is regulated by the synovium, a specialized connective soft-tissue membrane that lines the inner surface of synovial joint capsules [23]. The synovial fluid within the synovial cavity helps reduce friction, nourishes the joint structures, and provides shock absorption during movements of the knee joint.

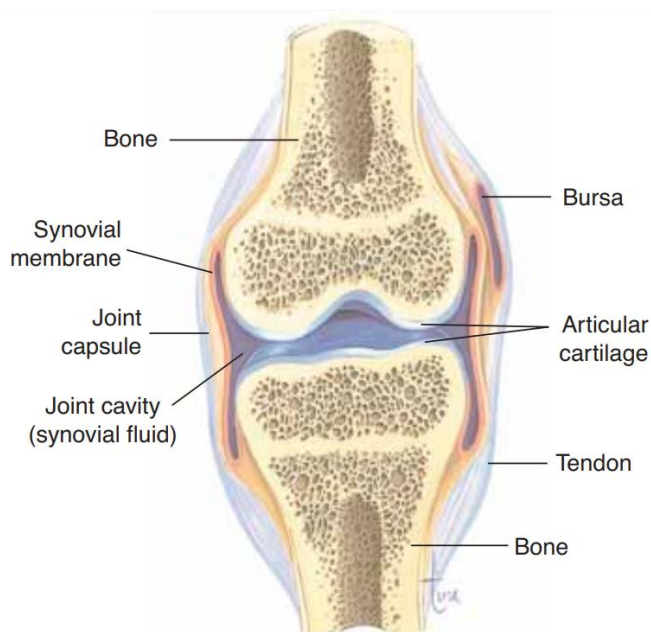


Figure 4: Synovial cavity of the knee joint [24].

On the joint surface of each bone is the articular cartilage, which provides a smooth surface. The joint capsule, made of fibrous connective tissue, encloses the joint in a strong sheath, like a sleeve. Lining the joint capsule is the synovial membrane, which secretes synovial fluid into the joint cavity. Synovial

fluid is thick and slippery and prevents friction as the bones move. Many synovial joints also have bursae (or bursas), which are small sacs of synovial fluid between the joint and the tendons that cross over the joint. Bursae permit the tendons to slide easily as the bones are moved. If a joint is used excessively, the bursae may become inflamed and painful; this condition is called bursitis [18].

The lubrication for the natural joint is provided by a small amount of viscous fluid consisting of mainly hyaluronic acid, proteins, and other factors such as lubricin and surface-active phospholipid (SAPL) that allow for effective gliding of the joints [25]. As with the tissue, the characteristics and properties of the fluid vary considerably as the result of joint health, injury status and other host factors such as inflammation and hypersensitivity. Injury to the joint may result in an abundance of fluid (a joint effusion), distension of the tissues and interruption of the normal functions of the synovial tissue [26].

Synovial fluid composition and visual characteristic are strongly dependent on the state of health of the patient, without any disorders the synovial fluid has egg white like consistency and colour [3]. In hemarthroses it will be red or orange and in inflammatory arthropathies may appear cream or white. Normal synovial fluid has a thick mucoid consistency because of complex interactions between proteins and proteoglycans. These interactions are fundamental to the lubricating properties of synovial fluid [27]. The synovial fluid was assumed to be a homogeneous and incompressible Newtonian fluid with a density of 1010 kg/m^3 and a dynamic viscosity of $0.008 \text{ kg/(m} \cdot \text{s)}$ [28].

4. Methodology

4.1. Geometry

The geometry has been created in SALOMÉ, an open-source software that provides a generic Pre- and Post-Processing platform for numerical simulation, including computational fluid dynamics (CFD) simulations. It is based on an open and flexible architecture made of reusable components [29]. It is designed to work with a variety of solvers, including OpenFOAM, Code Saturne, and others. Users can create complex geometries, mesh them, apply boundary conditions, and run CFD simulations. It also provides powerful post-processing tools to visualize and analyse simulation results. Salome uses an intuitive graphical user interface (GUI) and offers scripting capabilities using Python programming language, making it accessible to both novice and experienced users.

SALOME is a powerful and versatile tool for CFD simulations and has a wide range of functionalities and applications, for this study this open-source software has been used to create the geometry, and later mesh it. Once the geometry and the mesh are done, is it possible to export the mesh and geometry to UNV file, later a conversion should be carried out in order to be able to use the file in OpenFOAM, this process will be described in 4.4. Solver Section.

The project aims to simulate the whole knee joint, but a simplification has been done to reduce computational costs and have a first approach. Instead of studying the whole knee cavity, only one quarter of the cavity will be studied and simulated, the cavity of the medial condyle of the femur.

4.1.1. Geometry Improvement

The geometry of the newly built structure was based on the geometry of a previous study of this project [9], which has been used as a reference. However, the previous one had a large cavity which was not that much realistic. In the new design, this cavity has been significantly reduced to improve accuracy. Moreover, adjustments have been made to the cavity between the medial epicondyle and medial condyle to have a better approach of the femur geometry. This improvements in the geometry were performed in SALOME and the process will be further explained on the following chapter 4.1.2 Geometry Characterisation. The designed geometry represents the synovial cavity from adductor tubercle to the patellar surface, the right quarter side of the femur as shown in **Error! Reference source not found.**, that illustrates the lower side of the femur, with all its parts labelled.

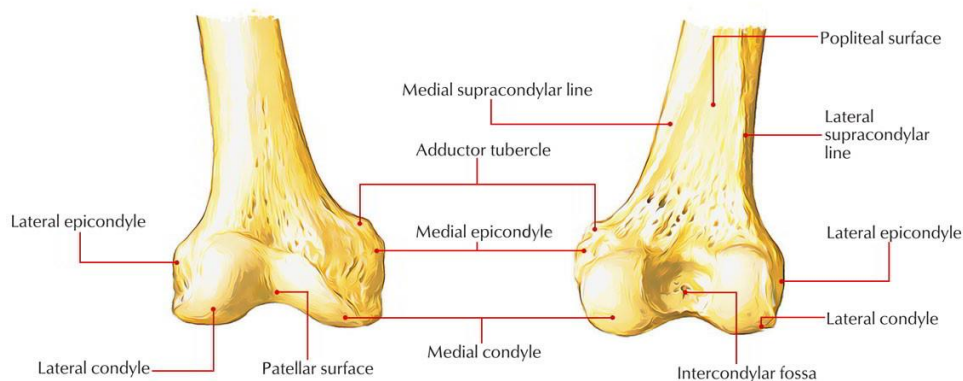


Figure 5: Lower part of the femur [30].

Figure 6 depicts a Magnetic Resonance Image (MRI) of the knee in a coronal plane, which was used to facilitate the design and improvement of the cavity's geometry. The image has been enhanced by overlaying the simulated cavity geometry, providing a visual representation of the modelled quarter of the knee cavity.

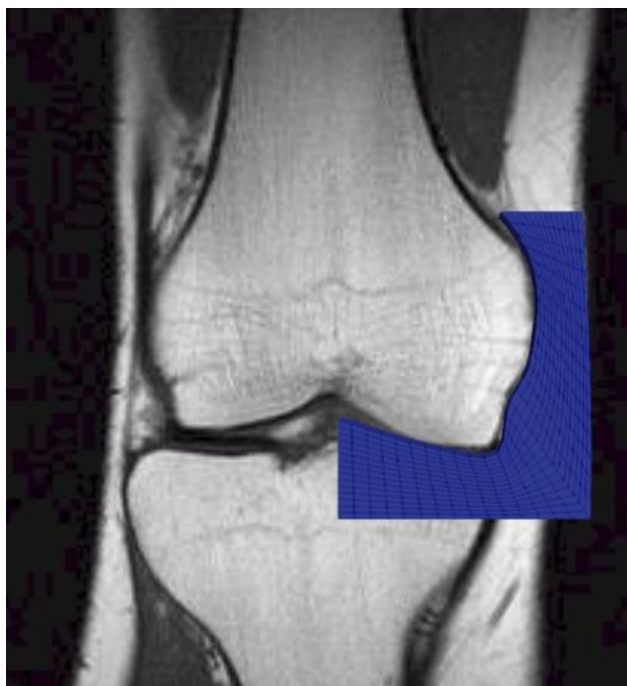


Figure 6: MRI of the knee and the cavity's geometry on top [31].

The dimensions of the cavity were determined based on the geometry from the previous study of the project [9], which measured 7cm x 5cm. However, adjustments were made to the geometry to improve the curvature and width of the cavity from the condyle and epicondyle. The resulting dimensions can be observed in Figure 7, dimensions are in International System of Units (m).

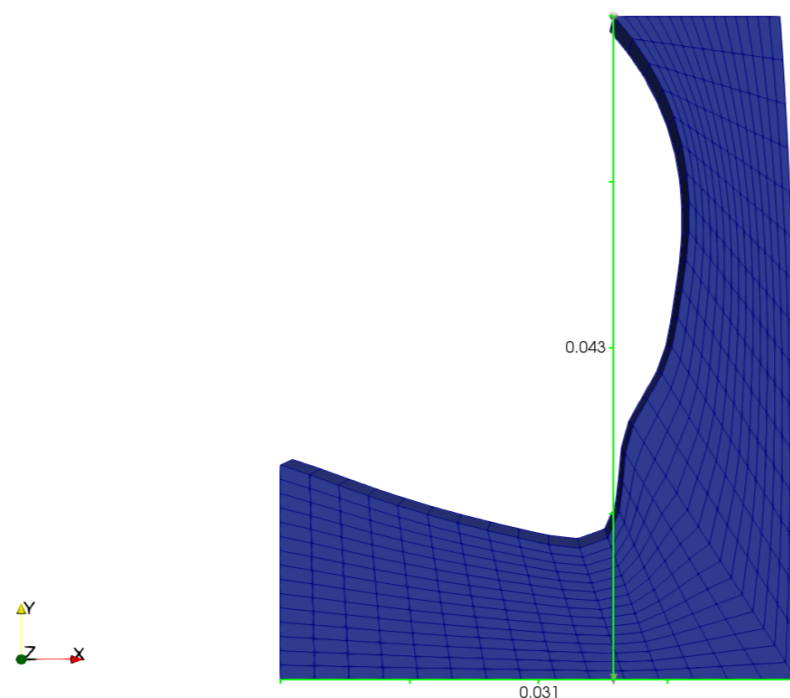


Figure 7: Dimensions of the quarter of the synovial cavity.

4.1.2. Geometry Characterisation

As mentioned before, the geometry was simplified to reduce computational costs, so instead of drawing the whole knee cavity, symmetry has been assumed and only one quarter of the cavity will be designed. To measure this quarter of the synovial cavity, a stereolithography (STL) file of the femur, a popular 3D printing technology, and a magnetic resonance image (MRI) of the knee in the coronal plane were used. By assigning different points on the STL file's curvature of the cavity and calculating the distances between them using SALOME's feature, a preliminary geometry was created. This geometry was then compared to the MRI of the knee, and few modifications were made to ensure that the points of the geometry obtained using the STL file corresponded to the points assigned in the MRI, as the STL file's geometries are divided into triangles, and this is not entirely precise when studying a curved cavity. Finally, the definitive second geometry was obtained after making these adjustments.

The geometry has been created using basic objects like points, which the user should define giving the coordinates to the system. Once the points were defined, those were joined using lines or splines for the curves. After that, a new face was created and extruded to form the cavity. Even though a 3D model was obtained, it is good to mention that the problem of study will be simplified in 2D, this will be done assigning specific boundary condition, empty, to front and back patches, whose plane is normal to the 2nd and 3rd dimension for which no solution is required. In Figure 8 the resulting geometry can be seen.

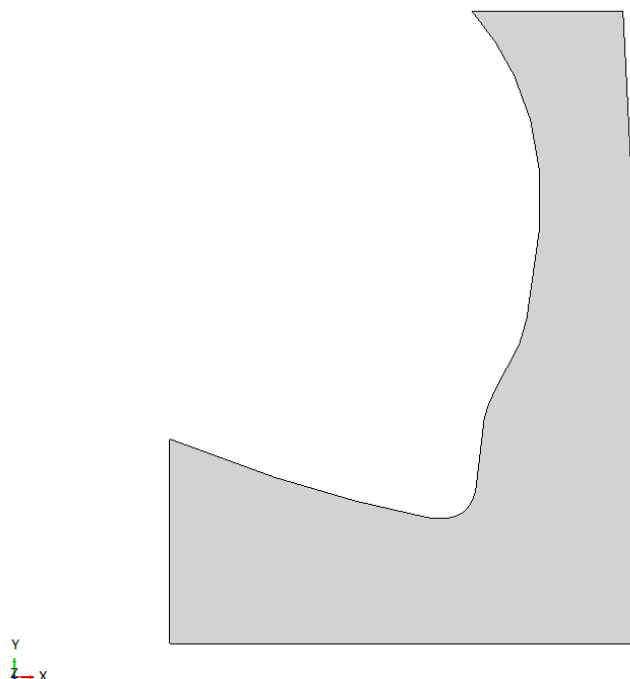


Figure 8: Resulting improved geometry in SALOME.

The geometry will be exploited by edges, this will create a list of sub-shapes, so that all edges of the 3D cavity can be named and later, sub-meshes with concrete specifications can be assigned to each edge. This will be further explained in 4.2 Mesh generation, the following chapter.

4.2. Mesh generation

Once the geometry is ready, next step is to mesh it. The open-source software SALOME offers a wide range of meshing tools, which can be used to generate structured or unstructured meshes. The user can also set different meshing properties depending on the requirements of the simulation. In the following sub-chapters, the meshing process will be explained.

4.2.1. Mesh Hypothesis

The mesh module in SALOME contains a set of meshing algorithms or hypothesis, which are used for meshing entities (1D, 2D, 3D sub-shapes) composing geometrical objects [29]. An algorithm represents either an implementation of a certain meshing technique or an interface to the whole meshing

program generating elements of several dimensions. In SALOME we can find different mesh hypothesis or algorithms:

- For meshing of 1D entities (edges):
 - *Wire Discretization* meshing algorithm: splits an edge into a number of mesh segments following an 1D hypothesis [29].
 - *Composite Side Discretization* algorithm: allows to apply a 1D hypothesis to a whole side of a geometrical face even if it is composed of several edges provided that they form C1 curve in all faces of the main shape [29].
- For meshing of 2D entities (faces):
 - *Triangle (Mefisto)* meshing algorithm: splits faces into triangular elements [29].
 - *Quadrangle (Mapping)* meshing algorithm: splits faces into quadrangular elements [29].
- For meshing of 3D entities (solid objects):
 - *Hexahedron (i,j,k)* meshing algorithm: solids are split into hexahedral elements thus forming a structured 3D mesh. The algorithm requires that 2D mesh generated on a solid could be considered as a mesh of a box, i.e. there should be eight nodes shared by three quadrangles and the rest nodes should be shared by four quadrangles [29].
 - *Body Fitting* meshing algorithm: solids are split into hexahedral elements forming a Cartesian grid; polyhedral and other types of elements are generated where the geometrical boundary intersects Cartesian cells [29].

First step to mesh the studied geometry is to create the mesh hypothesis, this will define the meshing parameters, such as element size, shape, and type among others. The previous studies have been taken as a reference to choose the types of mesh hypothesis, the following algorithms have been chosen: in 3D meshing the Hexahedron (i,j,k) was selected, in 2D meshing the algorithm Quadrangle: Mapping, and in 1D mesh Wire Discretization algorithm with an Hypothesis of Number of Segments, in order to define the number of mesh segments and distribution of the nodes.

The newly created hypothesis are applied to the geometry and later compute it to generate the mesh. Once the mesh is created, the user can get various information about it such as the number of nodes or segments. The mesh can be later visualized and edited if necessary.

4.2.2. Sub-meshes Construction

The sub-mesh is an object used to assign a sub-shape different meshing parameters than those assign to the main shape. Structurally, the sub-mesh is a mesh on a certain sub-shape, or a group of sub-shapes, possibly generated using different meshing algorithms and/or hypotheses than those used to

generate the mesh on other sub-shapes [16]. Creation of a sub-mesh allows to have certain control over the sub-shape mesh thus the segments of the mesh can be assigned per each edge, so that a locally coarser or finer mesh can be obtained.

In the case of study different sub-meshed have been applied in all boundaries. For example, in order to be able to process the model later in OpenFOAM, it is convenient that the mesh is as similar as possible to a 2D mesh, that is why in the z-coordinate the cell will be of one dimension as the stability of the mesh will depend on this. For this purpose, a sub-mesh with a number of segments equal to one has been created for all the edges in z-axis direction. Now the user can understand why it is important to explode the geometry by edges, so that different sub-shapes can be assigned. For the other cells, a specific number of segments has been also defined. In Figure 9, the resulting mesh can be seen. The mesh is structured and quadrilateral, structured because the domain is divided into a regular grid, and quadrilateral because it is partitioned using quadrilaterals.

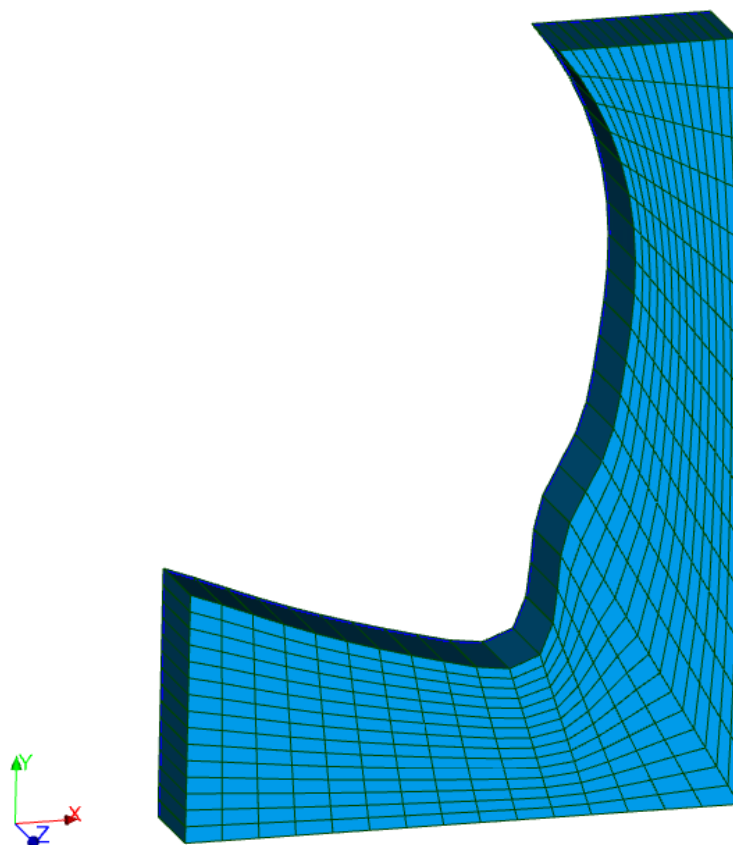


Figure 9: Resulting quadratic mesh from the improved geometry in SALOME.

4.2.3. Patches Creation

To be able to assign different properties to the different cells of the geometry, patches should be defined. Patches can be understood like each face on the surface that forms the surface geometry. In 4.3.1. Boundary Conditions section, basic types of patches will be explained.

The user can create these patches using SALOME feature: groups of sub-shapes of the geometry. A group can be formed by different types of elements such as nodes, faces or volumes among others. In the case of study, the groups will be created using faces as the element types and this groups can consist of one or more faces. All the groups can be named and by doing this, the user is later able to establish different boundary conditions, pressure, and velocity to each group in OpenFOAM software. In Figure 10 the different names for each group or patches can be seen as follows.

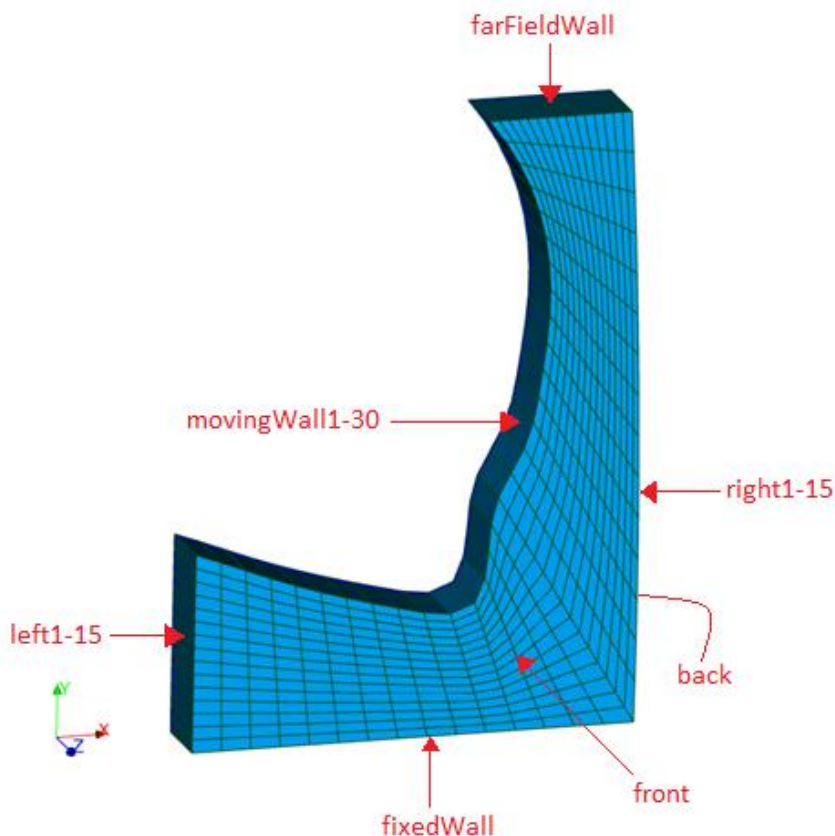


Figure 10: Resulting mesh with corresponding patches.

The cavity is divided into 7 main patches: *left*, *movingWall*, *farFieldWall*, *right*, *fixedWall*, *front* and *back*. Some of these main patches have been divided in cells (or other patches) to later be able to assign different velocities to each cell or patch. For example, *MovingWall* has been divided into 30 groups,

from *MovingWall1* to *MovingWall30*, so it is formed by 30 patches. *Left* and *right* have been divided into 15 groups or faces, and the others, *fixedWall*, front, back and *farFieldWall*, all boundary faces form one group or one patch. From now on in this study, when mentioning this groups, faces or cells, only the name of patches will be used.

4.2.4. Mesh Refinement

Mesh refinement is the process of improving the quality of a mesh by adding more vertices or adjusting the position of existing vertices. To do so, the user can use the Local Refinement option to refine specific areas of the mesh, or the Global Refinement option to refine the entire mesh.

In this study, the mesh refinement was in the global geometry and the process involved increasing the number of segments per edge to achieve smaller cell sizes, resulting in a higher cell count. The main goal was to get a smooth mesh with sufficiently small cells in the cavity of the femoral condyle, as the mesh refinement can increase the accuracy of the simulation by reducing numerical errors.

Once the mesh is done, the user can use an extra function in OpenFOAM to check the mesh quality. The following function has been used: *checkMesh*, which checks the validity of the mesh to ensure that the refined mesh has good topology and is free of errors.

4.2.5. Mesh Exportation

Last step is to export the mesh. SALOME offers various formats like UNV, MED and CGND, for use in numerical simulations. In this study the UNV format has been used and will be converted to Foam format, to be able to read it in OpenFOAM. In Algorithm 1, the command used can be seen, being *Mesh_1* the name of the geometry's file in SALOME.

```
ideasUnvToFoam Mesh_1.unv
```

Algorithm 1: Command to export the mesh to UNV format.

Running this command, a new folder named *constant* will be created. Inside this folder, another folder named *polyMesh* can be found, where all the information about the geometry can be obtained, including the *boundary* file where the user can see all the boundary patches and later edit the boundary conditions. This will be further explained in chapter 4.3.1. *Boundary conditions*.

4.3. Movement and Boundary Conditions

4.3.1. Boundary Conditions

Setting appropriate boundary conditions is vital for a successful simulation. Ill-posed boundary conditions will lead to physically incorrect predictions, and in many cases solver failure. Users must specify the boundary conditions for each solved field. We first need to consider that, for the purpose of applying boundary conditions, a boundary is generally broken up into a set of patches. One patch may include one or more enclosed areas of the boundary surface which do not necessarily need to be physically connected [32].

Basic patch types are:

patch

The basic patch type for a patch condition that contains no geometric or topological information about the mesh (with the exception of wall), e.g. an inlet or an outlet [32].

wall

There are instances where a patch that coincides with a wall needs to be identifiable as such, particularly where specialist modelling is applied at wall boundaries. A good example is wall turbulence modelling where a wall must be specified with a wall patch type, so that the distance from the wall of the cell centres next to the wall are stored as part of the patch [32].

symmetry

This boundary condition enforces a symmetry constraint. For any (non-planar) patch which uses the symmetry plane (slip) condition [32].

empty

While OpenFOAM always generates geometries in 3 dimensions, it can be instructed to solve in 2 (or 1) dimensions by specifying a special empty condition on each patch whose plane is normal to the 3rd (and 2nd) dimension for which no solution is required. For solutions in in 2 (or 1) dimensions (2D/1D), the type used on each patch whose plane is normal to the 3rd (and 2nd) dimension for which no solution is required [32].

In the case of study, a generic patch, *patch*, will be used as the condition for *movingWall*, *right*, and *farFieldWall*; *slip* condition for *left*; symmetry condition, *symmetry*, will be used for *fixedWall*; and

empty boundary condition for *front* and *back* patches. An example of the boundary file can be seen below in Setting 1 **Error! Reference source not found.**

```
(
  front
  {
    type          empty;
    nFaces        450;
    startFace     855;
  }
  back
  {
    type          empty;
    nFaces        450;
    startFace     1305;
  }
  fixedWall
  {
    type          symmetry;
    nFaces        15;
    startFace     1755;
  }
  farFieldWall
  {
    type          patch;
    nFaces        15;
    startFace     1770;
  }
  left1
  {
    type          slip;
    nFaces        1;
    startFace     1785;
  }
  ...
  movingWall1
  {
    type          patch;
    nFaces        1;
    startFace     1800;
  }
  ...
  right1
  {
    type          patch;
    nFaces        1;
    startFace     1830;
  }
  ...
)
```

Setting 1: Part of the boundary file in PolyMesh folder.

The patch types are specified in the mesh and field files of a OpenFOAM case. More precisely, the base type is specified under the type keyword for each patch in the boundary file, located in the constant/polyMesh directory [32]. In boundary file the base type is specified, this will be discussed in the following section.

4.3.2. Velocity and Pressure

In the *time directory* folder, a folder that contains the output files generated during a time-dependent OpenFOAM simulation, the user need to introduce all input data at the initial time step. Usually "0" will be defined as the initial time step. This input data will mainly be velocity and pressure definition but could contain other variables.

Boundary conditions in OpenFOAM are used to specify the values of variables of the computational domain such as velocity and pressure. To define parameters at the boundaries, the user should apply specific boundary condition types to each boundary face. Some basic boundary conditions to define those parameters are:

calculated

This boundary condition is not designed to be evaluated; it is assumed that the value is assigned via field assignment, and not via a call to e.g. updateCoeffs or evaluate [32].

fixedValue

This boundary condition supplies a fixed value constraint, and is the base class for a number of other boundary conditions [32].

zeroGradient

This boundary condition applies a zero-gradient condition from the patch internal field onto the patch faces. That means the gradient of respective quantity is zero, meaning that the actual value is constant [32].

totalPressure

This boundary condition provides a total pressure condition, is uniform total pressure applied everywhere in the inlet patch. Total pressure value is equal to p_0 [32].

movingWallVelocity

This boundary condition provides a velocity condition for cases with moving walls [32].

For the case of study, the boundary conditions used for velocity and pressure are shown in Table 1.

Table 1. Boundary conditions for each patch

Patch	U (velocity)	p (pressure)
left	slip	slip
movingWall	movingWallVelocity	totalPressure
farFieldWall	zeroGradient	zeroGradient
right	movingWallVelocity	zeroGradient
Back	empty	empty
front	empty	empty
fixedWall	symmetry	symmetry

In Setting 2 **Error! Reference source not found.**, part of the p file can be seen, where the user can add all boundary conditions regarding the pressure.

```

dimensions      [0 2 -2 0 0 0 0];

internalField   uniform 1000;

boundaryField
{
    movingWall1
    {
        type          totalPressure;
        p0            $internalField;
    }
    ...

    fixedWall
    {
        type          symmetry;
    }

    farFieldWall
    {
        type          zeroGradient;
    }

    left1
    {
        type          slip;
    }
    ...

```

```

    right1
    {
        type            zeroGradient;
    }
    ...

    back
    {
        type            empty;
    }

    front
    {
        type            empty;
    }
}

```

Setting 2: Part of the pressure file in 0 folder.

In Setting 3, part of the U file is shown, where the user can describe the boundary conditions related to the velocity.

```

dimensions      [0 1 -1 0 0 0 0];
internalField   uniform (0 0 0);

boundaryField
{
    movingWall1
    {
        type            movingWallVelocity;
        value            $internalField;
    }
    ...

    farFieldWall
    {
        type            zeroGradient;
    }

    fixedWall
    {
        type            symmetry;
    }

    left1
    {
        type            slip;
    }
    ...
}

```

```

right1
{
    type          movingWallVelocity;
    value         $internalField;
}
...
back
{
    type          empty;
}

front
{
    type          empty;
}
}
    
```

Setting 3: Part of the velocity file in 0 folder.

In U file, dimensions entry specifies the dimensions of the field. In Figure 11, it is shown how the system does work in OpenFOAM. For each position inside the bracket of dimensions a property is related and accordingly the unit. For example, in U file, dimensions $[0 1 -1 0 0 0 0]$; equals to $m \cdot s^{-1}$ that is the same as saying m/s, as there is a 1 in the second position (length) and -1 in third position (time).

No.	Property	SI unit	USCS unit
1	Mass	kilogram (kg)	pound-mass (lbm)
2	Length	metre (m)	foot (ft)
3	Time	— — — —	second (s) — — — —
4	Temperature	Kelvin (K)	degree Rankine (°R)
5	Quantity	— — — —	mole (mol) — — — —
6	Current	— — — —	ampere (A) — — — —
7	Luminous intensity	— — — —	candela (cd) — — — —

Figure 11: Unit system in OpenFOAM [33].

4.3.3. Velocity Calculation

In the study, the movement done by the knee when a human is walking is simulated. The walking gait can be divided into two main phases: stance (about 0-65% of gait) and swing phases (about 65-100% of gait) [34], [35]. The stance phase consists of three subphases: initial (heel strike to foot flat), middle (foot flat to opposite heel strike), and terminal stance (opposite heel strike to toe off) [35], [36]. The knee joint in the stance phase is regarded as a shock damping mechanism to accept the body weight

[37]. The swing phase consists of two subphases: initial (toe off to knee maximum flexion) and terminal swing (knee maximum flexion to heel strike) [35], [36]. The main function of the knee in the swing phase is assisting flexion-extension for toe clearance, foot placement, and taking over the load in the next step [38], [39]. To obtain the real movement of the knee the "Influence of musculoskeletal model parameter values on prediction of accurate knee contact forces during walking" [40] study has been used. This study uses a musculoskeletal model to predict knee contact forces during walking, and then vary the values of selected parameters to evaluate the sensitivity of the model to parameter changes. Throughout fluorescence experimentation and an algorithm, this study could obtain the translation between the femur and knee coordinate systems of a gait step, from heel strike to the next heel strike.

In the case of study, only vertical movement will be applied, and the horizontal translation will be simplified, considering that in the support phase, where the foot is in contact with the ground and supporting the body weight, there is no movement. Another simplification is that all the movements will be considered without acceleration, so all velocities will be lineal velocities. The total time of one gait cycle will be set to 1s, that is why the data taken from the study will be adjusted accordingly. The mesh will perform a cyclic movement to simulate the movement of the knee with a gait step, so the start point will be the same as the end point.

In the preceding study, the linear velocities were obtained from a velocity versus time graph constructed using data from the "Influence of musculoskeletal model parameter values on prediction of accurate knee contact forces during walking" study. The velocities were determined by calculating the slopes of the lines on the graph. In Figure 12, the velocities obtained at different times can be seen.

$$v = \begin{cases} 0 \text{ mm/s} & \text{for } 0 \text{ s} \leq t < 0,36 \text{ s} \\ -24,1065 \text{ mm/s} & \text{for } 0,36 \text{ s} \leq t < 0,53 \text{ s} \\ 11,7577 \text{ mm/s} & \text{for } 0,53 \text{ s} \leq t < 0,66 \text{ s} \\ -7,4775 \text{ mm/s} & \text{for } 0,66 \text{ s} \leq t < 0,74 \text{ s} \\ 12,1923 \text{ mm/s} & \text{for } 0,74 \text{ s} \leq t < 1 \text{ s} \\ 0 \text{ mm/s} & \text{for } t = 1 \text{ s} \end{cases}$$

Figure 12: Velocity values for one cycle of 1s.

At the beginning of the simulation, there is no movement until $t=0.36$ s, where the velocity reaches a negative value of 24.1 mm/s. From $t=0.36$ s to $t=0.53$ s, the velocity increases to 11.7 mm/s. Then, at $t=0.66$ s, it changes to a negative velocity of 7.5 mm/s, which persists until $t=0.74$ s. From $t=0.74$ s to $t=1$ s, the velocity increases again to 12.2 mm/s. Finally, at $t=1$ s, the velocity is set to 0 to close the cycle and prepare for the next iteration, ensuring that the start and end points match to maintain a cyclic pattern.

To prevent excessive compression or deformation of the bottom cells, which would not be compatible with our mesh, we will distribute the velocities across the patches. This will involve assigning higher

velocities to the upper patches and gradually decreasing them. For instance, in the MovingWall patches, the first patch, MovingWall1 (on the top side), will have higher velocity compared to MovingWall2, and MovingWall2 will have higher velocity compared to MovingWall3, and so on. Consequently, the lowest velocity of MovingWall patches will be found on MovingWall30, which is the last patch of the MovingWall. Regarding the left patches, left1 will initially have the same velocity as the neighbour patch, MovingWall30, and the velocities will progressively decrease until left15, where the velocity becomes 0. This is because the fixedWall has no velocity, hence its name. The same procedure will be applied to all the right patches. As for the farFieldWall, all the patches will have the same velocity as their neighbouring patches, MovingWall30 on the left side and right1 on the right side.

These velocities will be added to the *pointMotionUy* file, as the movement is happening in y-direction, inside of the initial time step ("0") in the *time directory* folder. The velocities profile will be set as in Setting 4.

```

dimensions      [0 1 -1 0 0 0 0];

internalField   uniform 0;

boundaryField
{
  movingWall1
  {
    type          uniformFixedValue;
    uniformValue  table
    (
      (0.0 0.0)
      (0.359 0.0)
      (0.36 -0.0241)
      (0.529 -0.0241)
      (0.53 0.0117)
      (0.659 0.0117)
      (0.66 -0.0075)
      (0.739 -0.0075)
      (0.74 0.0122)
      (0.999 0.0122)
      (1.0 0.0)
    );
  }
  ...
  movingWall30
  {
    type          uniformFixedValue;
    uniformValue  table
    (
      (0.0 0.0)
      (0.359 0.0)
      (0.36 -0.0098)
      (0.529 -0.0098)
      (0.53 0.0048)
      (0.659 0.0048)
    );
  }
}

```

```
(0.66 -0.0030)
(0.739 -0.0030)
(0.74 0.0050)
(0.999 0.0050)
(1.0 0.0)
);
}

right1
{
  type          uniformFixedValue;
  uniformValue  table
  (
    (0.0 0.0)
    (0.359 0.0)
    (0.36 -0.0241)
    (0.529 -0.0241)
    (0.53 0.0117)
    (0.659 0.0117)
    (0.66 -0.0075)
    (0.739 -0.0075)
    (0.74 0.0122)
    (1.0 0.0)
  );
}

right2
{
  type          uniformFixedValue;
  uniformValue  table
  (
    (0.0 0.0)
    (0.359 0.0)
    (0.36 -0.0223)
    (0.529 -0.0223)
    (0.53 0.01082)
    (0.659 0.01082)
    (0.66 -0.00693)
    (0.739 -0.00693)
    (0.74 0.01128)
    (0.999 0.01128)
    (1.0 0.0)
  );
}

....
right15
{
  type          uniformFixedValue;
  uniformValue  constant 0.0;
}

farFieldWall
{
  type          uniformFixedValue;
  uniformValue  table
  (
```

```

        (0.0 0.0)
        (0.359 0.0)
        (0.36 -0.0241)
        (0.529 -0.0241)
        (0.53 0.0117)
        (0.659 0.0117)
        (0.66 -0.0075)
        (0.739 -0.0075)
        (0.74 0.0122)
        (0.999 0.0122)
        (1.0 0.0)
    );
}

fixedWall
{
    type          uniformFixedValue;
    uniformValue  constant 0.0;
}

left1
{
    type          uniformFixedValue;
    uniformValue  table
    (
        (0.0 0.0)
        (0.359 0.0)
        (0.36 -0.0093)
        (0.529 -0.0093)
        (0.53 0.0045)
        (0.659 0.0045)
        (0.66 -0.0029)
        (0.739 -0.0029)
        (0.74 0.0047)
        (0.999 0.0047)
        (1.0 0.0)
    );
}

left2
{
    type          uniformFixedValue;
    uniformValue  table
    (
        (0.0 0.0)
        (0.359 0.0)
        (0.36 -0.00862)
        (0.529 -0.00862)
        (0.53 0.00417)
        (0.659 0.00417)
        (0.66 -0.00269)
        (0.739 -0.00269)
        (0.74 0.00436)
        (0.999 0.00436)
        (1.0 0.0)
    );
}

...

```

```

left15
{
    type            uniformFixedValue;
    uniformValue    constant 0.0;
}

back
{
    type            empty;
}

front
{
    type            empty;
}
}

```

Setting 4: Velocity profile for some of the patches.

4.3.4. Simulation Parameter Definition

Apart from the mesh generation and initial boundary condition, some physical conditions should be introduced in the system in order to run the simulation. The user should also input data relating to the control of time.

This viscosity is a single value which is constant in time and uniform over the solution domain [41]. This value has been searched on the literature, where it has been found that the synovial fluid has a density similar to that of egg white, as its composition and visual characteristic are strongly dependent on the state of health of the patient, without any disorders the synovial fluid has egg white like consistency and colour [3]. The synovial fluid was assumed to be a homogeneous and incompressible Newtonian fluid with a density of 1010 kg/m^3 and a dynamic viscosity of $0.008 \text{ kg/(m} \cdot \text{s)}$ [28].

As mentioned above, the input in OpenFOAM is the kinematic viscosity, this can be calculated as dynamic viscosity (μ) divided by density (ρ) as shown in Eq. (1):

$$\text{nu} = \nu = \frac{\mu}{\rho} = \frac{8 \cdot 10^{-3} \text{ N} \cdot \text{s/m}^3}{1010 \text{ kg/m}^3} = 7,9208 \cdot 10^{-6} \text{ m}^2/\text{s} \quad (1)$$

The physical properties for the case are stored in dictionary files in the constant directory. In the case of study, the input data is introduced in file as shown in Setting 5 **Error! Reference source not found.**:

```

transportModel Newtonian;

nu            [0 2 -1 0 0 0] 7.9208e-06;

```

Setting 5: Input of kinematic viscosity.

The physical properties for the fluid are specified in *TransportProperties* file, respectively, in the constant directory. The Newtonian transport model is selected, i.e., representing it as a Newtonian fluid with a kinematic viscosity specified by the *nu* keyword in units $\text{N} \cdot \text{m}^{-1}$ ($= \text{m}^2 \cdot \text{s}^{-1}$).

Input data relating to the control of time and reading and writing of the solution data are read in from the controlDict dictionary [41]. This file is also located in the system directory. The user is able to define the start and stop times, and the time steps for the run can also be set. In the case of study the start`Time` is specified to be 0 and end`Time` 1. To achieve temporal accuracy and numerical stability when running the simulation, the time step, represented by the keyword `deltaT`, should be defined in such a way that a CFL number of less than 1 is achieved. This ensures that the simulation accurately captures the dynamics of the system while maintaining stability.

The convergence and stability of numerical schemes was initially addressed by Courant, Friedrichs, and Lewy (CFL) [42]. They showed that in order for the solution of a difference equation to converge to the solution of the partial differential equation the numerical scheme must use all the information contained in the initial data that influence the solution [43]. The Courant number (also referred as Co or CFL) is a dimensionless quantity that relates the time step (`deltaT`), the speed of wave propagation (*U*), and the spatial discretization in the simulation (`deltaX`). The Courant number can be calculated as shown in Eq. (2):

$$Co = \frac{|U| \cdot \delta t}{\delta x} < 1 \quad (2)$$

where:

$|U|$ is the magnitude of the velocity through that cell

δt is the time step

δx is the spatial grid size in the direction of the velocity

By keeping the Courant number below 1, we can avoid numerical instabilities and ensure reliable results. To achieve temporal accuracy and numerical stability when running the simulation, the time step, represented by the keyword `deltaT`, will be defined making sure that a Courant number of less than 1 is achieved.

To write results at certain intervals of time, so that the user can later view with a post-processing package, the `writeControl` keyword will be used. This presents several options for setting the time at which the results are written; here the `timeStep` option will be selected, which specifies that results are written every *n*th time step where the value *n* is specified under the `writeInterval` keyword [41]. OpenFOAM creates a new directory named after the current time, e.g. 0.1 s, on each occasion that it writes a set of data. For the case of study, the time cycle is 1 s and the time step is every 100 intervals,

that means a written file will be saved every 0.01 s, creating 100 files in total. The entries in the controlDict are shown below in Setting 6 **Error! Reference source not found.**

```
application      pimpleFoam;
startFrom        startTime;
startTime        0;
stopAt           endTime;
endTime          1;
deltaT           1.0e-4;
writeControl     timeStep;
writeInterval    100;
purgeWrite       0;
writeFormat      binary;
writePrecision   6;
writeCompression off;
timeFormat       general;
timePrecision    6;
runTimeModifiable true;

functions
{
    #include "cuttingPlane"
}
```

Setting 6: ControlDict File.

In the system directory the fvSchemes and fvSolution dictionaries are also to be found. The user can specify the choice of finite volume discretization schemes and the linear equation solvers and tolerances, as well as other algorithms controls can be made also made in those dictionaries. The user is free to view these dictionaries, but we do not need to discuss all their entries at this stage [41].

By modifying the values of the parameters within the dictionaries, the user can alter the absolute pressure field in the simulation. However, it should be noted that the relative pressures and velocity field cannot be changed directly. In a closed incompressible system like a cavity, the absolute pressure values are not significant; instead, it is the pressure differences or pressure ranges that hold

importance. Therefore, at this stage, the absolute pressure values will not be further discussed since they do not impact the simulation outcome significantly.

4.4. Solver

The solvers for Computational Fluid Dynamics (CFD) in OpenFOAM are based on the Navier-Stokes equations, which are a set of partial differential equations that describe the motion of incompressible fluids, based on conservation laws. There are two commonly used approaches to describing conservation laws: the Eulerian approach and the Lagrangian approach. In the Eulerian approach, the conservation laws are described in terms of fixed points in space, so focuses on a specific volume element through which the fluid flows over time, on the other hand, in the Lagrangian approach, they are described in the perspective of individual particles, that means each particle is tracked individually as it moves through space and time. Figure 13 provides a schematic illustration, offering a visual explanation.

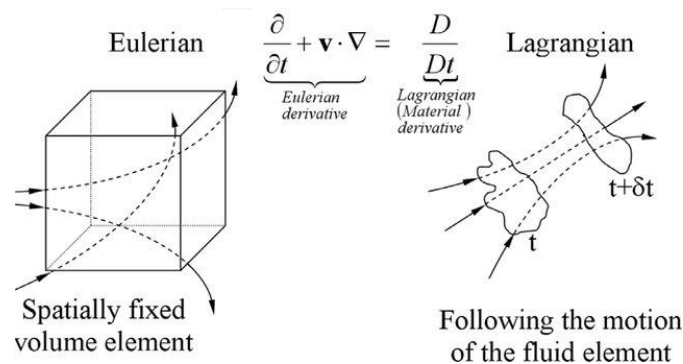


Figure 13: Eulerian and Lagrangian representation of fluid flow equations [44].

4.4.1. Navier-Stokes Equations

The Navier-Stokes equations describe the fluid flow by the continuity, momentum and energy equations. These equations govern the conservation of mass, which is based on the continuity equation, in Eq. (3); conservation of momentum, based on the Newton's Second Law, in Eq. (4); and conservation of energy, based on the First Law of Thermodynamics or Energy Equation, in Eq. (5) and can be written in a general form as follows:

$$\frac{\partial \rho}{\partial t} + \nabla \cdot (\rho \cdot \bar{U}) = 0 \quad (3)$$

$$\frac{\partial(\rho \cdot \bar{U})}{\partial t} + \nabla \cdot (\rho \cdot U \cdot U) = -\nabla \cdot P + \nabla \cdot \tau \quad (4)$$

$$\frac{\partial(\rho \cdot E)}{\partial t} + \nabla \cdot (\rho \cdot \bar{U} \cdot E) = -\nabla \cdot \dot{q}_s - \nabla \cdot (\rho \cdot \bar{U}) + \nabla \cdot (\tau \cdot \bar{U}) + f_b \cdot \bar{U} + \dot{q}_V \quad (5)$$

where:

ρ is the density of the fluid

U is the velocity vector of the fluid

P is the pressure of the fluid

τ is the stress tensor of the fluid

E is the total energy of the fluid

\dot{q}_s is the rate of heat transfer per unit area across the surface area of the material element

\dot{q}_V represents the rate of heat source within the material volume per unit volume

T is the temperature of the fluid

f_b is the body forces.

4.4.1.1. Mass Conservation

The mass in the control volume can be neither created nor destroyed, it can only be transported from one region to another. The conservation of the mass states that the mass flow difference throughout the system is zero, that can be seen in Eq. (3):

$$\frac{\partial \rho}{\partial t} + \nabla \cdot (\rho \cdot \bar{U}) = 0 \quad (3)$$

The first term on the left-hand side represents the time rate of change of density, while the second term represents the divergence of the mass flux vector. The gradient operator ∇ is described in Eq. (6):

$$\bar{\nabla} = \bar{i} \frac{\partial}{\partial x} + \bar{j} \frac{\partial}{\partial y} + \bar{k} \frac{\partial}{\partial z} \quad (6)$$

Assuming the fluid is incompressible, where the density remains constant, the continuity equation can be simplified to represent a steady-state process, as shown in Eq. (7):

$$\frac{\partial \rho}{\partial t} = 0 \rightarrow \nabla \cdot \bar{U} = \frac{\partial u}{\partial x} + \frac{\partial v}{\partial y} + \frac{\partial w}{\partial z} \quad (7)$$

4.4.1.2. Momentum Conservation

Momentum describes a mass in motion and is measured as the product between an object's mass and velocity. As the momentum in control volume remains constant, the conservation of momentum implies momentum is neither created nor destroyed. It can only change through the action of forces based on Newton's law [45].

$$\frac{\partial(\rho \cdot \bar{U})}{\partial t} + \nabla \cdot (\rho \cdot \bar{U} \cdot \bar{U}) = -\nabla \cdot P + \nabla \cdot \tau \quad (4)$$

Eq. (4) describes the conservation of momentum of the fluid. The first term on the left-hand side represents the time rate of change of momentum, while the second term represents the convection of momentum. The first term on the right-hand side represents the pressure gradient force, while the second term represents the viscous forces acting on the fluid, which for some cases of study can be omitted. The description is set up in accordance with the Eq. (8), the expression of Newton's Second Law of Motion:

$$F = m \cdot a \quad (8)$$

where:

F is the net force applied to the object

m is the mass of the object

a is the resulting acceleration of the object

4.4.1.3. Energy Conservation

Conservation of energy is the first law of thermodynamics which states that the sum of the work and heat added to the system will result in an increase in the total energy of the system [45], this is described in Eq. (5):

$$\frac{\partial(\rho \cdot E)}{\partial t} + \nabla \cdot (\rho \cdot \bar{U} \cdot E) = -\nabla \cdot \dot{q}_s - \nabla \cdot (\rho \cdot \bar{U}) + \nabla \cdot (\tau \cdot \bar{U}) + f_b \cdot \bar{U} + \dot{q}_v \quad (5)$$

The first term on the left-hand side represents the time rate of change of total energy of the fluid, the second term represents the convective transport of energy. The first term on the right-hand side represents the conductive heat transfer within the fluid and last term represents any heat generation of absorption per unit of volume.

The first law of thermodynamic equation, Eq. (9), can be described as follows:

$$dE_t = dQ + dW \quad (9)$$

where dQ is the heat added to the system, dW is the net work on the system, and dE_t is the increment in the total energy of the system.

4.4.2. PimpleFoam

The PIMPLE algorithm is a numerical algorithm for solving the Navier-Stokes equations in OpenFOAM. PIMPLE stands for "Pressure-Implicit with Splitting of Operators" and is a combination of the SIMPLE (Semi-Implicit Method for Pressure-Linked Equations) and PISO (Pressure-Implicit with Splitting of Operators) algorithms. Both algorithms, the pressure-implicit split-operator (PISO) or semi-implicit method for pressure-linked equations (SIMPLE) are iterative procedures for solving equations for velocity and pressure, PISO being used for transient problems and SIMPLE for steady-state [46]. Both algorithms are based on evaluating initial solutions and subsequently correcting them. However, the algorithms differ in the number of corrections they perform. In the SIMPLE algorithm a pressure correction term is used while the velocity corrections are neglected because they are unknown. This results in rather slow convergence. The PISO algorithm also neglects the velocity correction in the first step, but then performs one in a later stage, which leads to additional corrections for the pressure [47].

The PIMPLE algorithm uses a segregated approach to solve for the pressure and velocity fields in a time-marching manner. It iteratively solves the momentum equations (using the PISO algorithm) and the pressure-correction equation (using the SIMPLE algorithm) until convergence is achieved. The PIMPLE algorithm also allows for the use of adaptive time-stepping and under-relaxation factors, which can improve the stability and convergence of the solution. This algorithm is suitable for simulating incompressible and transient fluids, as well as handling turbulence and finite volume options. The input requirements for this algorithm include the kinematic pressure and the initial velocity.

4.5. Post-Processing

OpenFOAM is supplied with a post-processing utility paraFoam that uses ParaView, an open-source visualisation application. ParaView operates a tree-based structure in which data can be filtered from the top-level case module to create sets of sub-modules. The strength of ParaView is that the user can create a number of sub-modules and display whichever ones they feel to create the desired image or animation [48].

4.5.1. ParaView

In the post-processing step, the simulation results can be visualized and analysed using ParaView, an open-source visualization tool. ParaView offers various options for visualizing data in different formats and provides a wide range of tools for analysis and exploration. Users can generate plots, graphs, and other visual representations to gain insights into the simulation results and understand the behaviour of the system being simulated.

5. Results and Analysis

To analyse the results as mentioned before, the post-processing tool of OpenFOAM, ParaView, has been used. The primary focus of analysis for this project will be on velocity profiles, as they provide valuable insights into the flow patterns and characteristics within the simulated knee cavity. In addition to velocity profiles, other relevant parameters will also be analysed to further support the correctness of the simulation and enhance our understanding of the fluid dynamics in the synovial cavity.

By conducting a comprehensive analysis of these parameters, we aim to demonstrate the fidelity and reliability of the simulation results. The findings will be presented and discussed in this section and plots, graphs, and visualizations will be presented to illustrate the key findings.

5.1. Effect of Viscosity on Pressure Results

To see the relationship between the pressure and the kinematic viscosity in our model, three different kinematic viscosities (ν) have been taken and introduced into the same model:

- $\nu_1 = 4,95 \cdot 10^{-5} \text{ m}^2/\text{s}$
- $\nu_2 = 1 \cdot 10^{-3} \text{ m}^2/\text{s}$
- $\nu_3 = 1,5 \cdot 10^{-3} \text{ m}^2/\text{s}$

As described in the methodology section, the estimated value of the synovial fluid viscosity was adopted based on the literature. Then the viscosity was increased to see its impact on the physical properties. In this case, the effect of the viscosity variations on the pressure within the system was studied.

Following, the pressure maps for the three different kinematic viscosity cases are presented. These color-coded maps illustrate the distribution of pressure throughout the geometry. Extracted from the model at time 0,36s of the gait cycle, this specific time corresponds to the transition from the stance phase to the swing phase. It represents the compression of the synovial cavity due to the femur movement towards the cavity. The image displays the pressure ranges for each case on the right side.

It is important to note that OpenFOAM calculates pressure relative to density, which means that the observed values should be multiplied by the fluid density (1010 kg/m^3). However, it is worth emphasizing that the focus is not solely on the absolute value but rather on the range of values obtained. The results obtained are the following:

For $\nu_{u_1} = 4,95 \cdot 10^{-5} \text{ m}^2/\text{s}$ the range of pressures obtain can be observed in Figure 14.

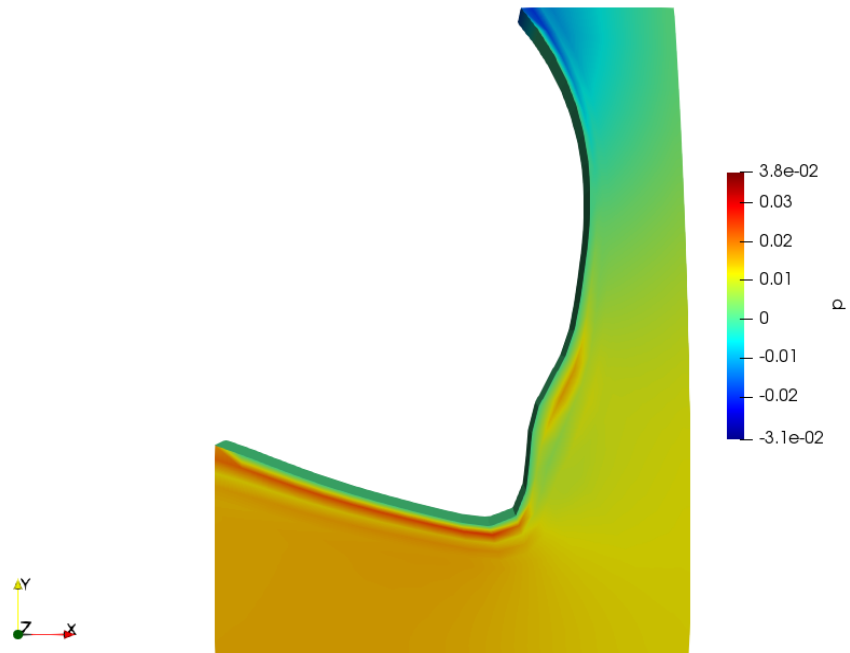


Figure 14: Pressure map for nu 1 at 0,36 s.

For $\nu_{u_2} = 1 \cdot 10^{-3} \text{ m}^2/\text{s}$ the range of pressures obtain can be seen in Figure 15.

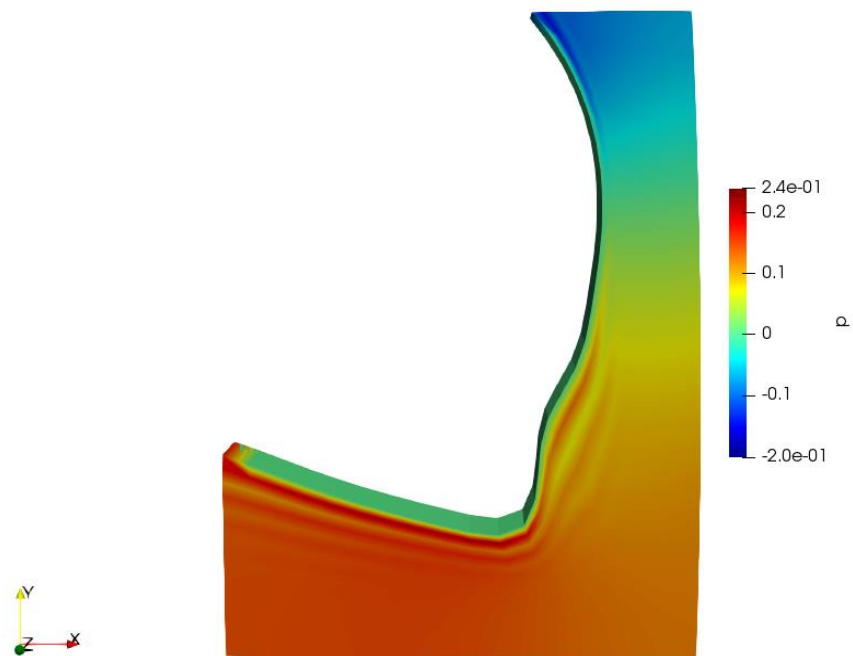


Figure 15: Pressure map for nu 2 at 0,36 s.

For $\nu_3 = 1,5 \cdot 10^{-3} \text{ m}^2/\text{s}$ the range of pressures obtain can be seen in Figure 16.

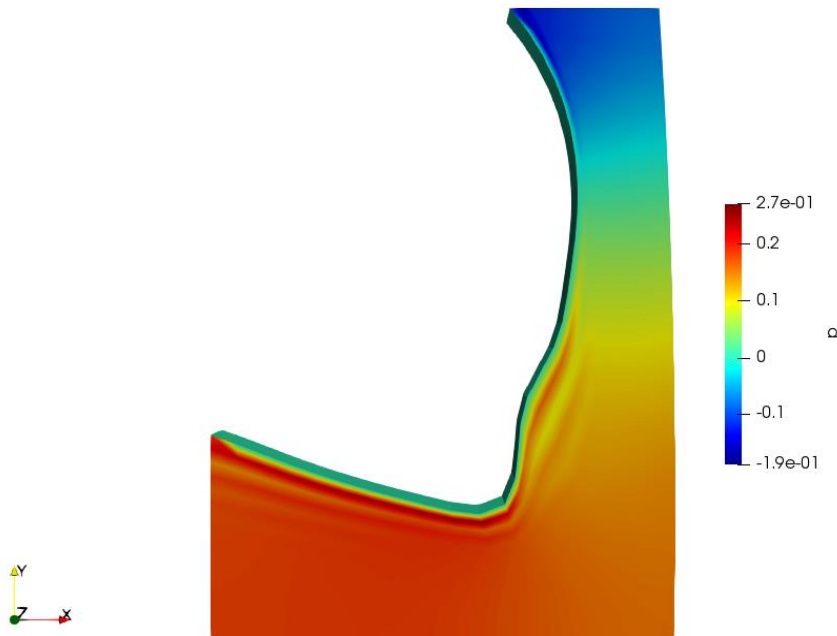


Figure 16: Pressure map for nu 3 at 0,36 s.

In Figure 14, the maximum pressure relative to density is observed to be $0,038 \text{ Pa} \cdot (\text{kg}/\text{m}^3)$ for the case of $\nu_1 = 4,95 \cdot 10^{-5} \text{ m}^2/\text{s}$. The highest pressure value is located just below the medial condyle of the femur, where the synovial fluid is being compressed due to the bone movement.

When the kinematic viscosity is increased to $\nu_2 = 1 \cdot 10^{-3} \text{ m}^2/\text{s}$, the corresponding effect on pressure relative to the density of the fluid is also an increase, reaching $0,24 \text{ Pa} \cdot (\text{kg}/\text{m}^3)$, as depicted in Figure 15. Finally, further increase on the kinematic viscosity, $\nu_3 = 1,5 \cdot 10^{-3} \text{ m}^2/\text{s}$, lead to higher pressure relative to density, as shown in Figure 16, where the relative pressure reaches a value of $0,27 \text{ Pa} \cdot \text{kg} \cdot \text{m}^{-3}$.

The results were as expected, as the effect of viscosity on pressure can be understood through the concept of resistance to flow. When the viscosity of the fluid increases, it becomes more resistant to flow. This increased resistance hinders the movement of the fluid particles, resulting in higher internal friction within the fluid. As a result, the pressure within the system increases.

The influence of viscosity on pressure can be attributed to the higher intermolecular forces of attraction associated with increased fluid viscosity. Consequently, the available free volume within the cavity decreases due to compression and the molecules experience reduced freedom of movement, resulting in higher internal friction forces.

5.2. Volume Results

The volume can be calculated using the “Integrate Variable” in ParaView and selecting the desired variable to integrate. For volume calculation, “1” can be chosen as the integration variable. This corresponds to integrating a constant value of 1 over the domain, effectively calculating the volume. The volume of the fully expanded cavity reached a value of $2,9215 \cdot 10^{-6} \text{ m}^3$, whereas the maximum compression, occurring at 0.53 s, resulted in a volume of $2,5166 \cdot 10^{-6} \text{ m}^3$. Figure 17 displays a plot illustrating the variation in percentage in the volume of the cavity.

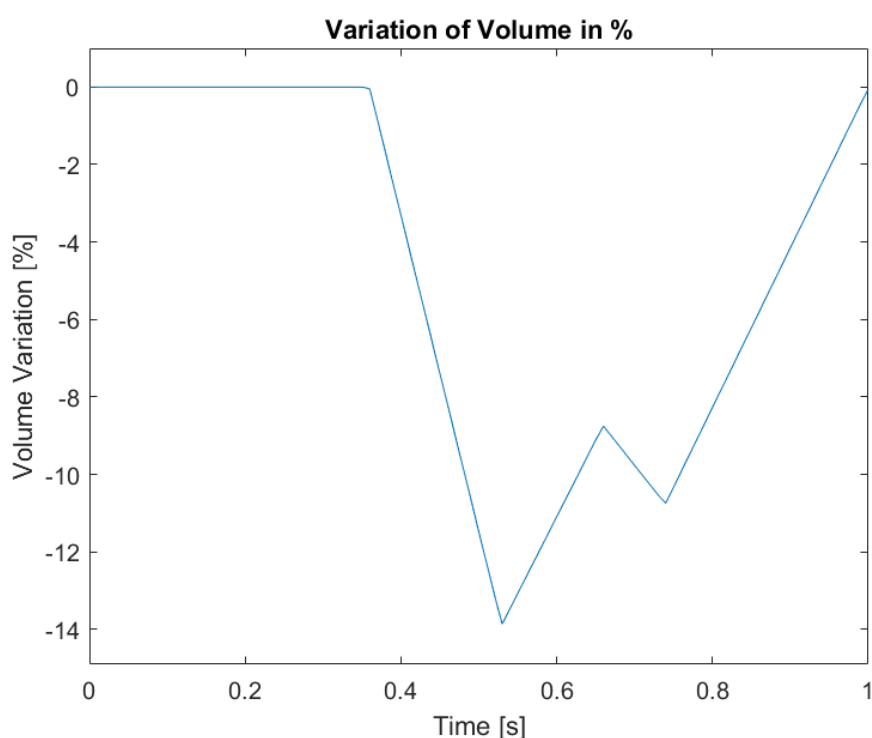


Figure 17: Variation of volume during a gait cycle.

As anticipated, the volume of the synovial cavity undergoes changes throughout the gait cycle, specifically during the initial swing phase. At 0.36 s, the cavity experiences the first compression due to the bone movement, resulting in a 14% decrease in the volume, as the femur moves downward in the y-axis direction. This compression continues until 0.53 s, when the femur starts moving upward, causing the volume of the cavity to expand again. In comparison with the non-compressed cavity, more than 8% of volume loss is observed. The last contraction of the cavity occurs at 0.66 s, corresponding to the terminal swing phase. During this phase, the volume decreases by 11% compared to the initial state. At 0.74 s, the volume expands once again. The gait cycle concludes at 1 s, with the cavity fully expanded, restoring the volume to its initial state.

5.3. Velocity Results

To analyse the velocity results, ParaView plot over a line function will be used. This feature enables the user to plot data values probed along a line through the dataset. In this case, six vertical lines will be defined at various positions all over the geometry, as seen in Figure 18.

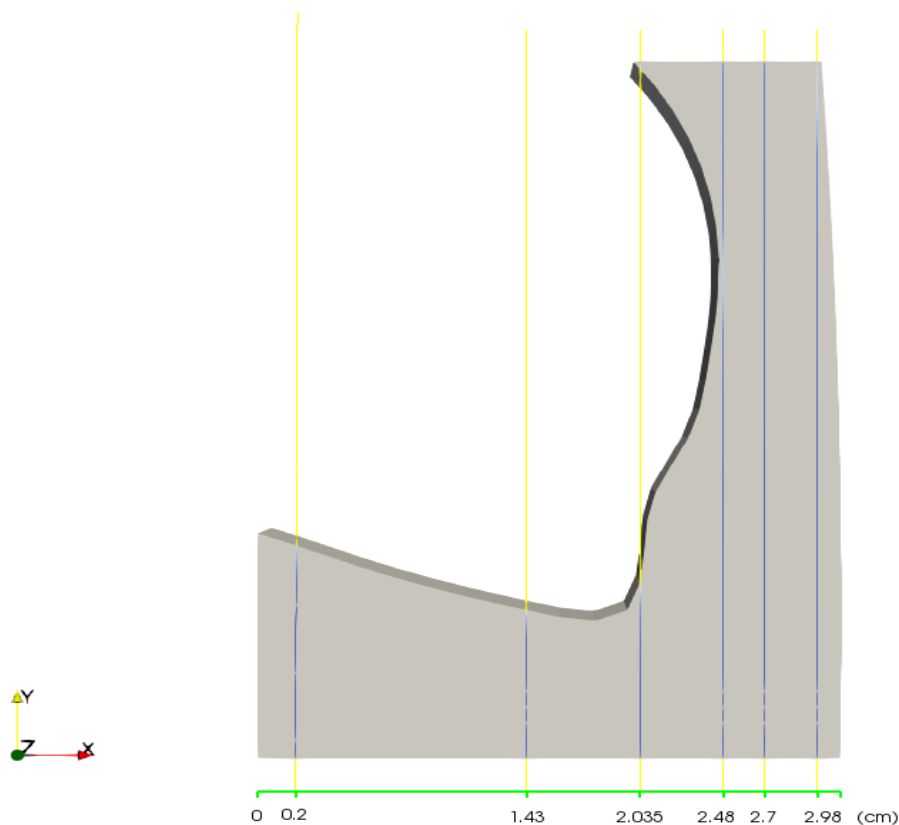


Figure 18: Geometry with the lines to plot the velocity.

These lines have been distributed along the x-axis, with the x position per each line listed below. The lines cross the entire geometry vertically, blue lines on Figure 18, and they are positioned in the midpoint of the z-axis (0.25 cm). Exact position for the lines can be seen as follows:

- Position 1 in x-axis: 0.2 cm
- Position 2 in x-axis: 1.43 cm
- Position 3 in x-axis: 2.035 cm
- Position 4 in x-axis: 2.48 cm
- Position 5 in x-axis: 2.7 cm
- Position 6 in x-axis: 2.98 cm

To facilitate the identification of these lines on the plots, the legend will display the x-axis position, and each case will be assigned a consistent colour across all velocity results plots.

5.3.1. Magnitude of Velocity

The magnitude of velocity has been studied for 5 different time steps: 0.36 s, 0.53 s, 0.62 s, 0.74 s and 0.9 s. In Figure 19, the magnitude of velocity at 0.36 s can be seen for the different lines going across the geometry.

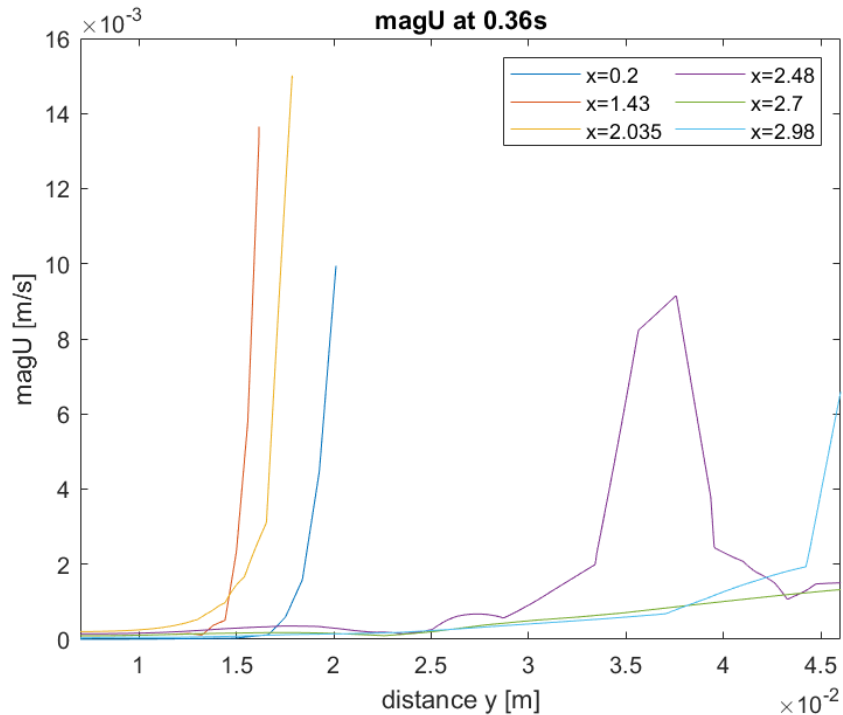


Figure 19: Magnitude of velocity at 0.36 s.

As the cavity is compressed due to the movement of the femur at 0.36 s, the liquid is expelled towards the lateral part of the cavity. This motion is depicted in the first three curves, which represent the lower part of the cavity. In these curves, the velocity of the liquid reaches a maximum of 1 to 15 mm/s. In the purple curve, specifically at $x=2.48$ cm, the liquid remains still until 2.5 cm, after which it starts accelerating, reaching an approximate velocity of 10 mm/s. In the other curves, a gradual increase in velocity is observed, indicating that the fluid is not significantly affected during the initial compression of the cavity. Regarding the behaviour of the fluid in the lateral region of the cavity, the fluid is slightly accelerated at positions $x=2.7$ cm and $x=2.98$ cm. However, at $x=2.48$ cm, which is the closest line to the lateral part of the femur, the fluid is more accelerated, reaching speeds of up to 9 mm/s.

Figure 20 will display the colour map representing the magnitude of velocity for a time step of 0.36 s. To facilitate visual comparison of the coloured maps across different time steps in the simulation, a consistent scale range will be applied to all colour maps.

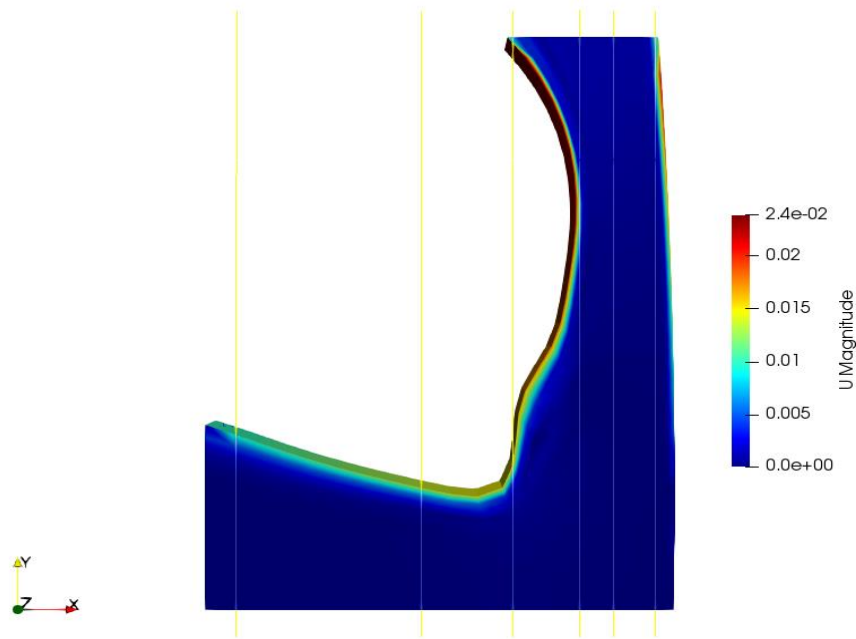


Figure 20: Coloured map of magnitude of velocity at 0.36 s.

The movement begins at this time frame, which is why the maximum velocity is observed at the surrounding of MovingWall boundary where the cells first come into contact with the bone. As a result, the liquid starts to be pushed in the negative y-axis direction.

Figure 21 displays the velocities for 0.53 s, when maximum compression of the cavity occurs.

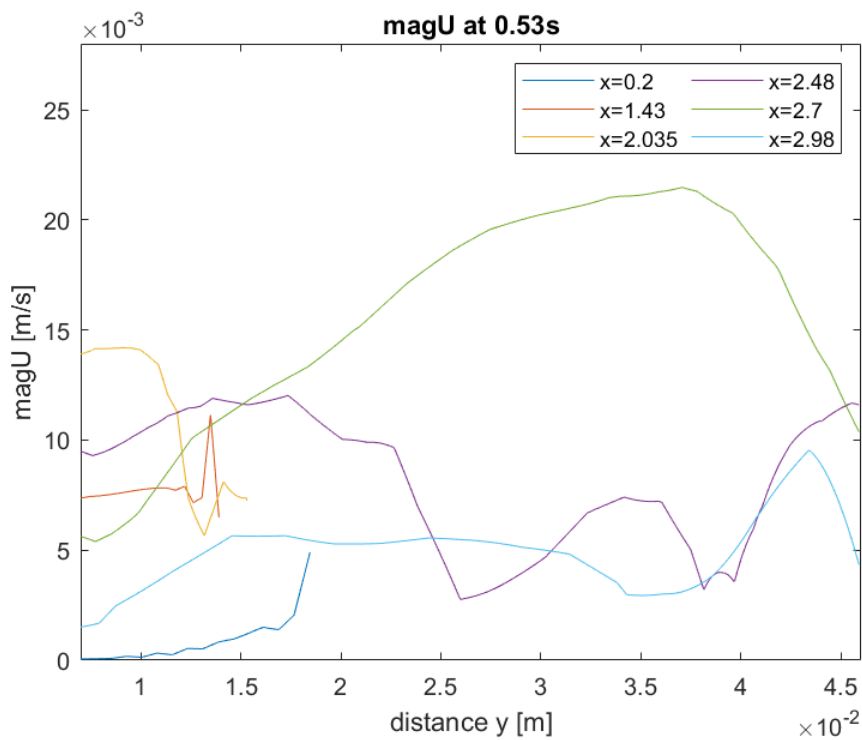


Figure 21: Magnitude of velocity at 0.53 s.

During this time, a parabolic velocity profile can be observed at $x=2.7$ cm, with the maximum velocity occurring near the medial epicondyle, which is the most curved part of the femur. In the other lines within the lateral region of the cavity, the velocity profile is not parabolic, indicating that the fluid continues to change direction. Following, Figure 22Error! Reference source not found. shows the coloured map of magnitude velocity.

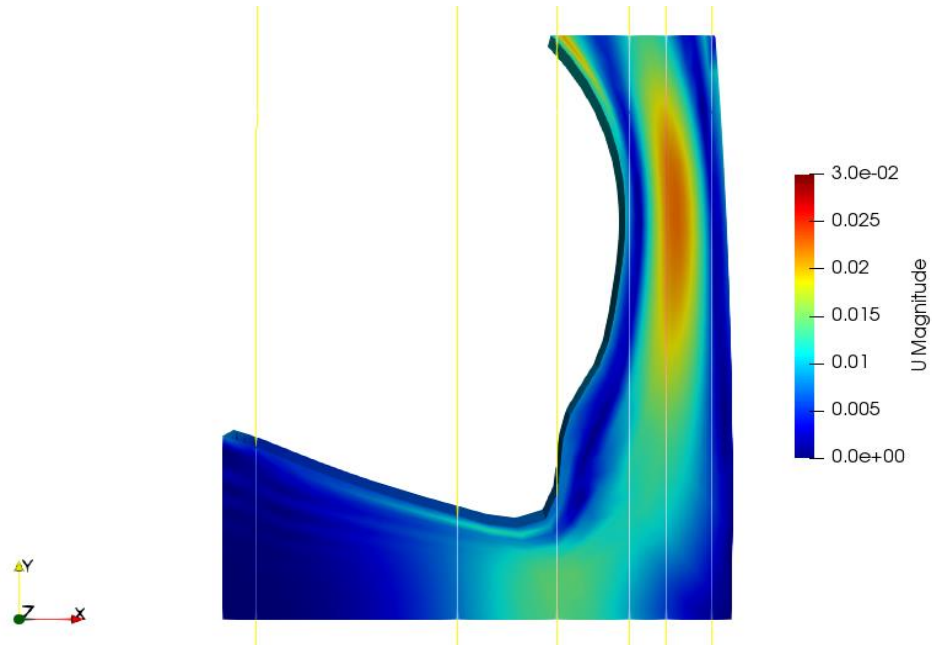


Figure 22: Coloured map of magnitude of velocity at 0.53 s.

At 0.62 s, the bone movement has changed direction. In Figure 23, the velocity profiles can be seen.

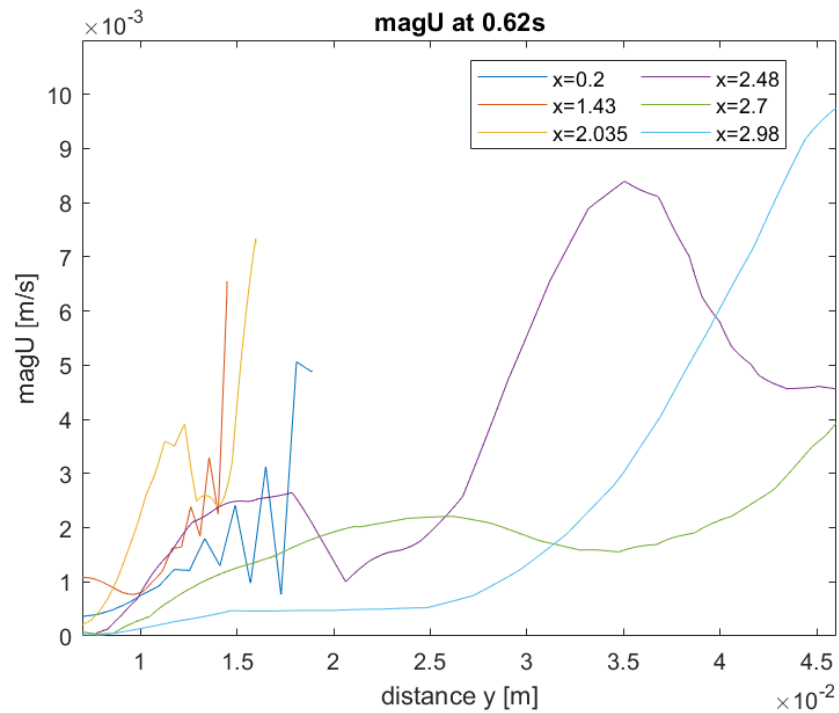


Figure 23: Magnitude of velocity at 0.62 s.

At 0.62 s, changes in velocity direction can be observed in the bottom part of the cavity. On the lateral side of the cavity, the fluid exhibits bigger velocities, particularly in the upper side of movingWall and right boundaries, where velocities around 9mm/s are reached (Figure 24).

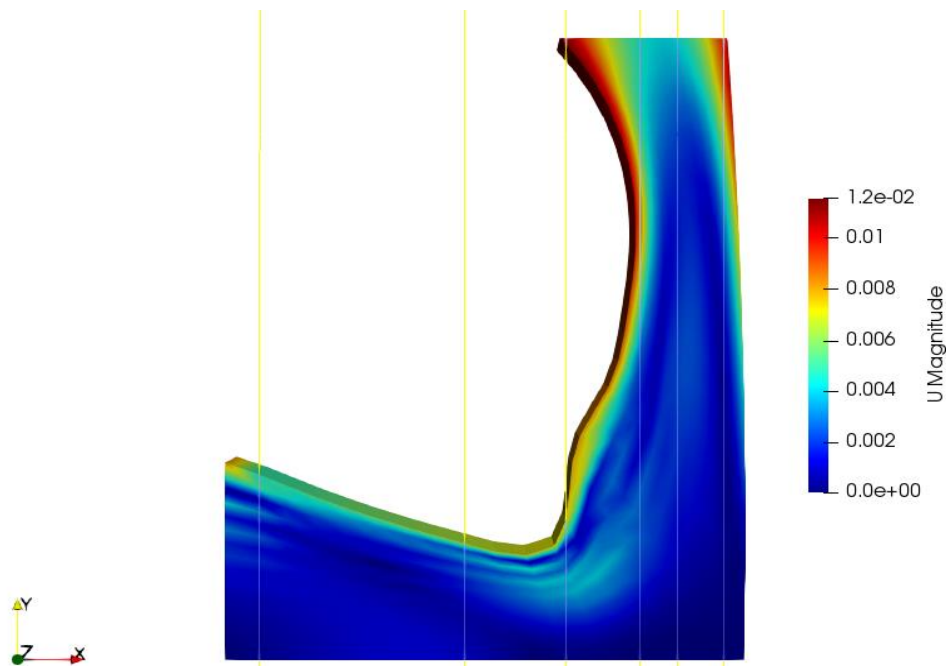


Figure 24: Coloured map of magnitude of velocity at 0.62 s.

At 0.74 s, the femur moves down again, resulting in compression of the cavity and high velocities near the movingWall boundary and in the middle of the lateral cavity (Figure 25).

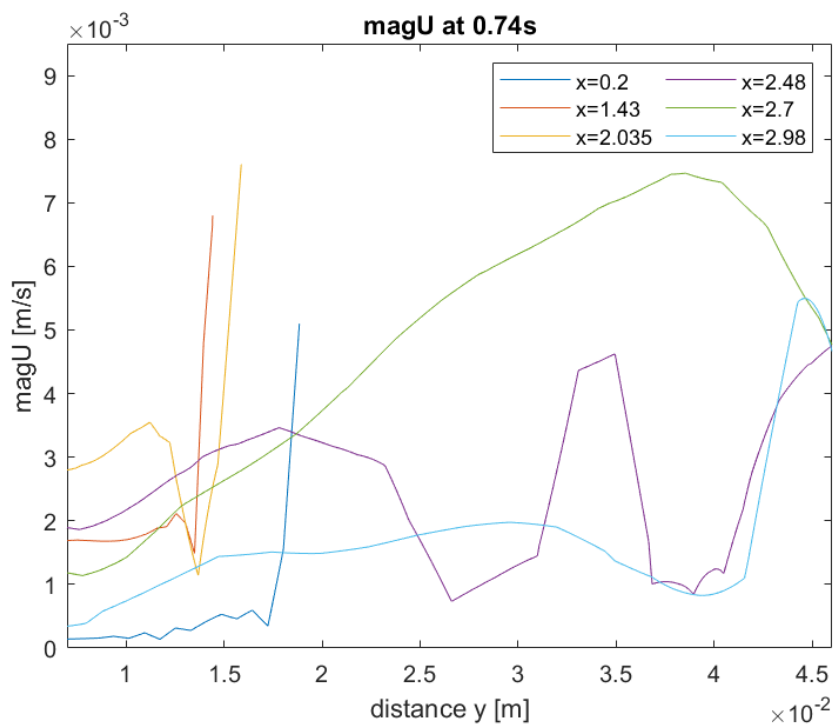


Figure 25: Magnitude of velocity at 0.74 s.

As a result of the compression, in the bottom part of the cavity the velocity of the synovial fluid increments significantly. However, the highest velocities are found in the lateral side, in $x=2.7$ cm a parabolic velocity profile can be seen, and in the movingWall and top right boundary (Figure 26).

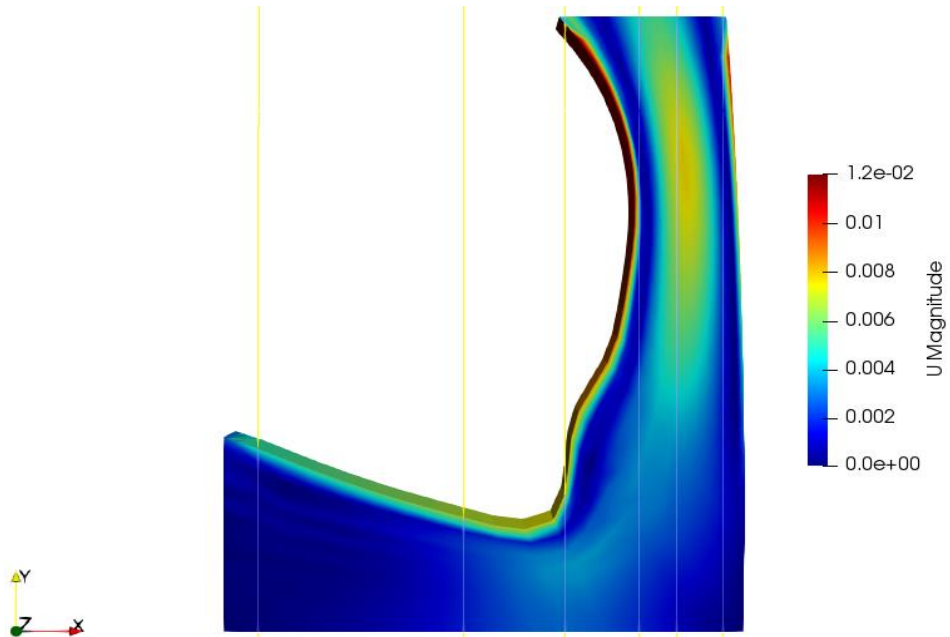


Figure 26: Coloured map of magnitude of velocity at 0.74 s.

At 0.90 s, the femur is moving upwards as the simulation cycle approaches its end, which concludes at 1 s. The velocity of the upwards movement of the femur is around 12 mm/s, while in the fluid motion, velocities up to 8 mm/s are found (Figure 27).

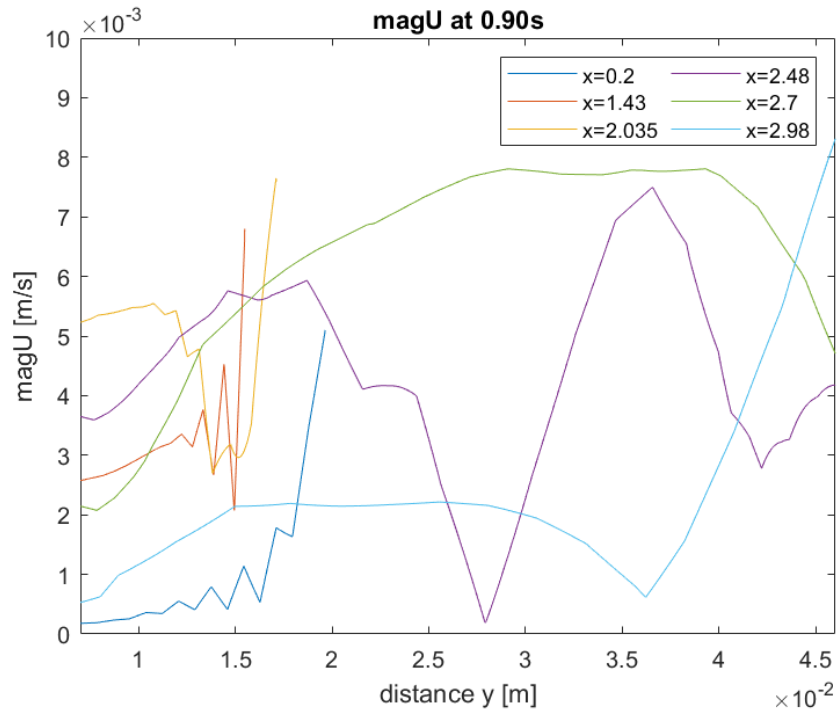


Figure 27: Magnitude of velocity at 0.90 s.

The fluid near the movingWall boundary is getting high velocities, particularly in the medial epicondyle and adductor tubercle side. In the middle of the lateral side of the cavity, high velocities can also be observed (Figure 28).

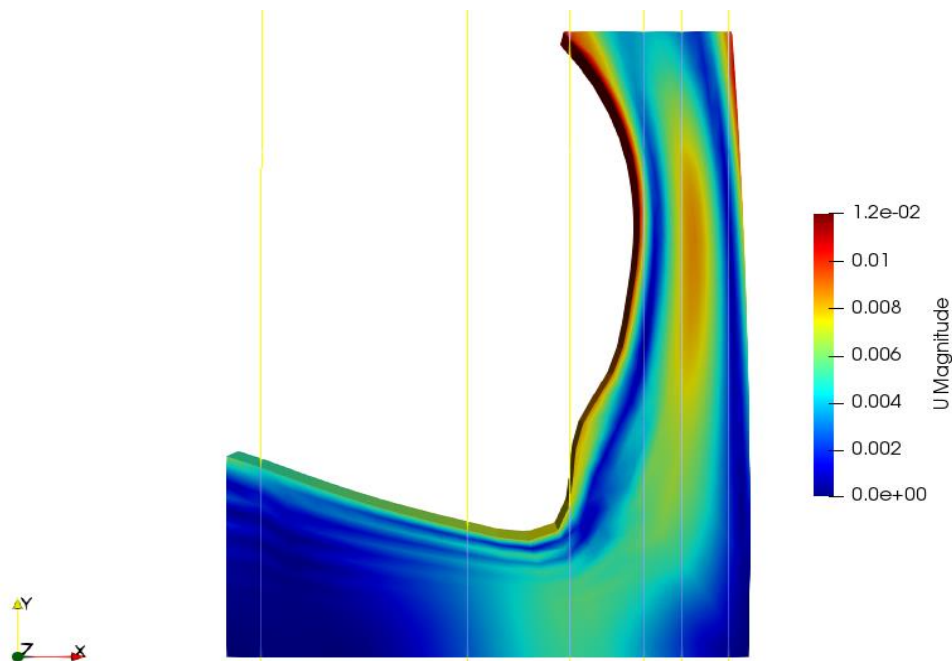


Figure 28: Coloured map of magnitude of velocity at 0.90 s.

In general, it can be observed that the highest magnitudes of velocities are found near the movingWall boundary, where the bone acts as a wall, pushing the fluid outwards. Additionally, high velocities have been observed in the upper side of the right boundary. These right patches are also acting as a wall, propelling the fluid in the direction of motion. Additionally, in certain instances, a parabolic velocity profile has been observed in the middle of the lateral side of the cavity, with the highest velocities occurring near the medial epicondyle of the femur.

5.3.2. X-direction Velocity (U_x)

In this sub-chapter, the results for the component of velocity in the x-direction will be showed. This represents the velocity of the synovial fluid along the horizontal axis. V_x velocity has also been studied for 5 different time steps: 0.36 s, 0.53 s, 0.62 s, 0.74 s and 0.9 s. In this case, since the velocities vary significantly depending on the time step, the scale of the coloured maps has been adjusted for each time step for a better visual overview.

Figure 29 displays the velocity U_x at 0.36 s. During this time, the femur initiates a downward movement, leading to the compression of the cavity.

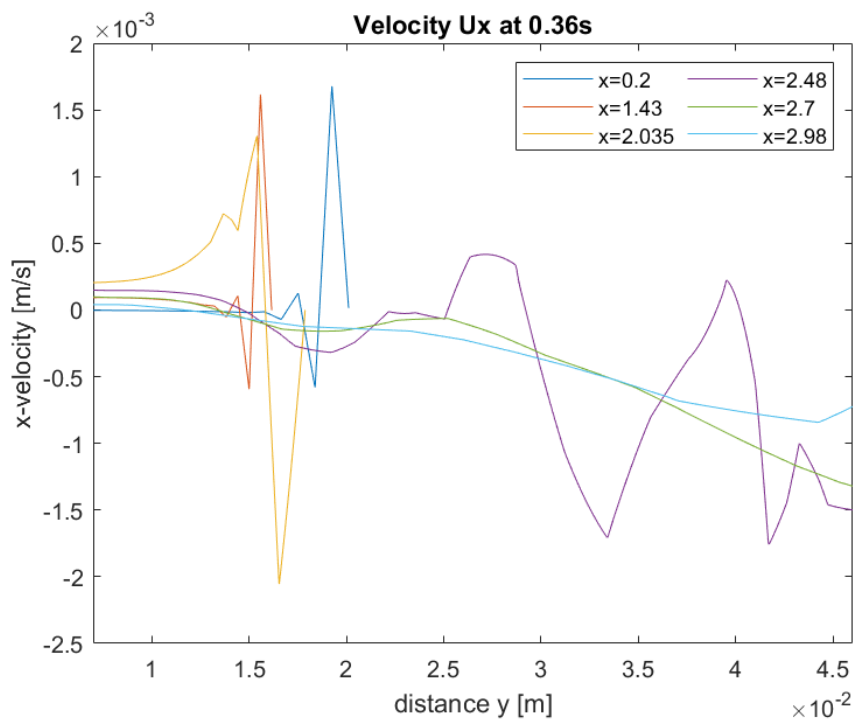


Figure 29: X-axis velocity at 0.36 s.

The fluid in the bottom part gets velocity, especially in proximity to the boundary, where the contact with the femur occurs. Figure 30 shows the slight change in velocity near the boundary, with the maximum velocity observed in the upper side of the movingWall boundary.

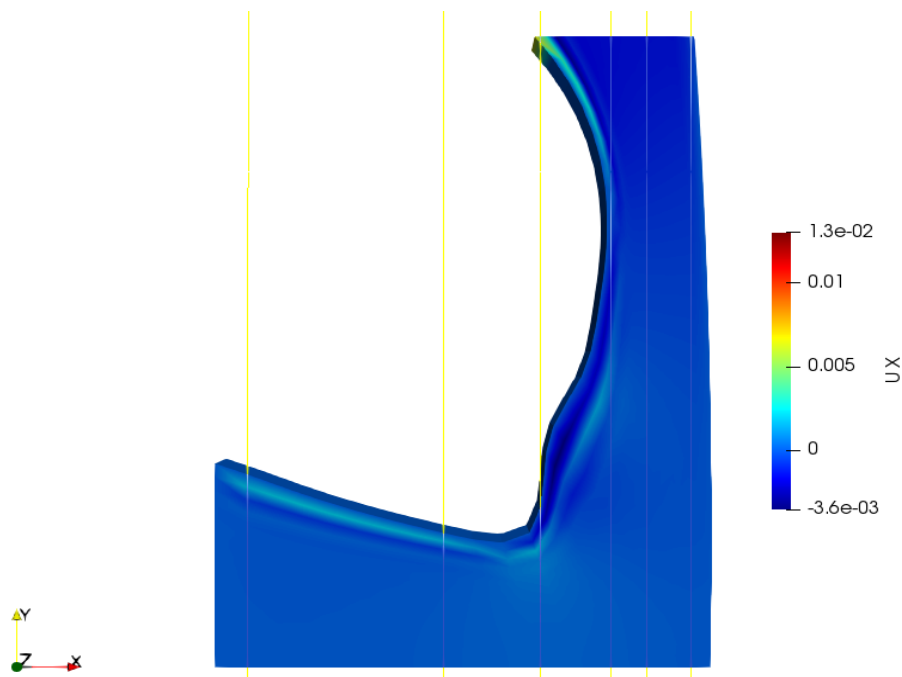


Figure 30: Coloured map of x-axis velocity at 0.36 s.

Comparing it to the previous timeframe, the U_x velocity values at 0.53 s are almost 10 times higher (Figure 31). This significant increase in velocity is attributed to the maximum compression of the cavity, resulting in the expulsion of fluid in the positive x-direction.

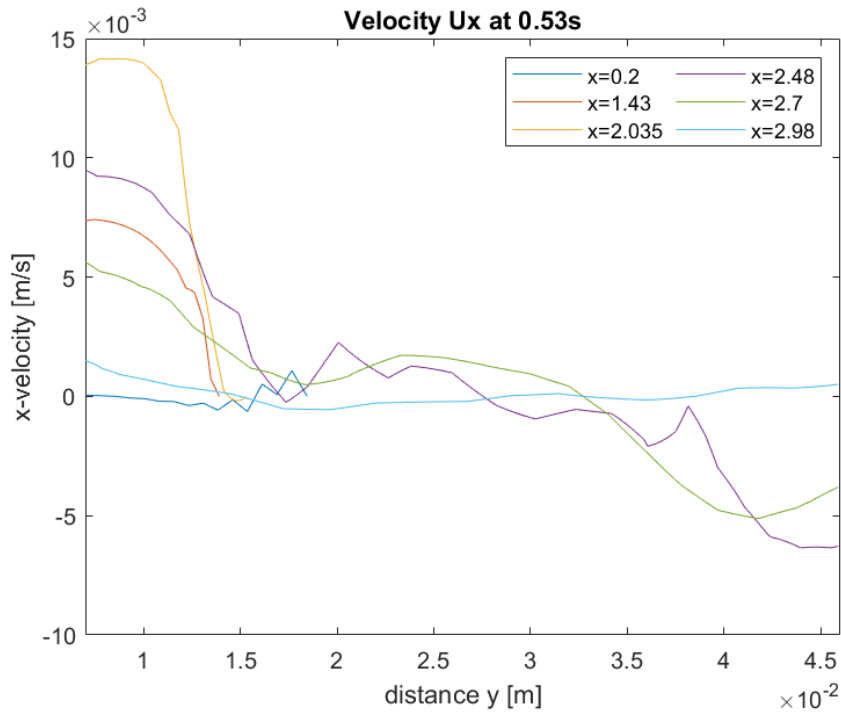


Figure 31: X-axis velocity at 0.53 s.

Maximum velocities in the bottom side of the cavity, in the femur medial condyle, where the fluid is being expelled towards the lateral cavity are observed (Figure 32).

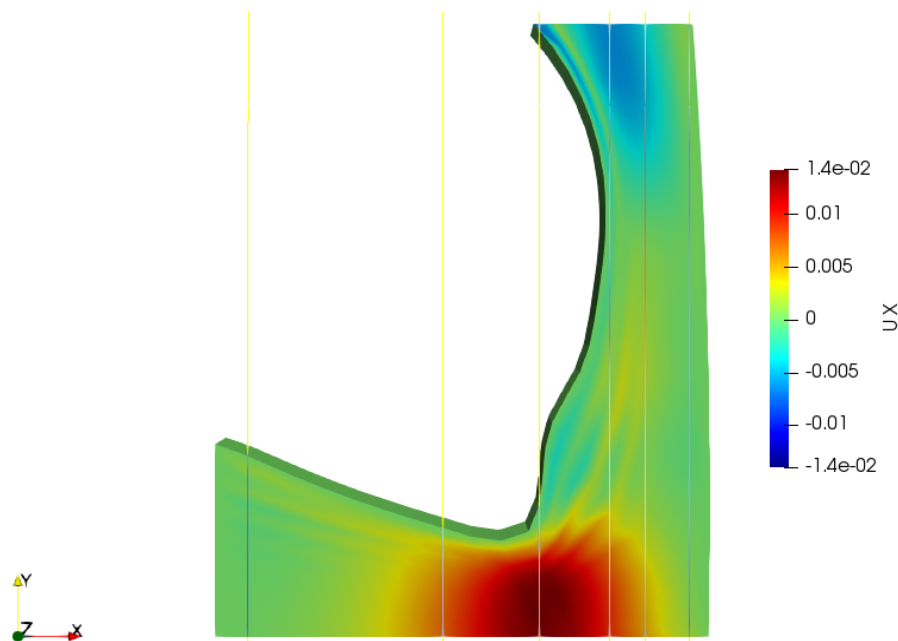


Figure 32: Coloured map of x-axis velocity at 0.53 s.

At time step 0.62 s, the cavity experiences expansion, leading to a decrease in fluid velocity. The flow direction changes near the medial condyle, moving towards the left boundary. In the lateral cavity, the highest velocities are observed at the movingWall boundary (Figure 33).

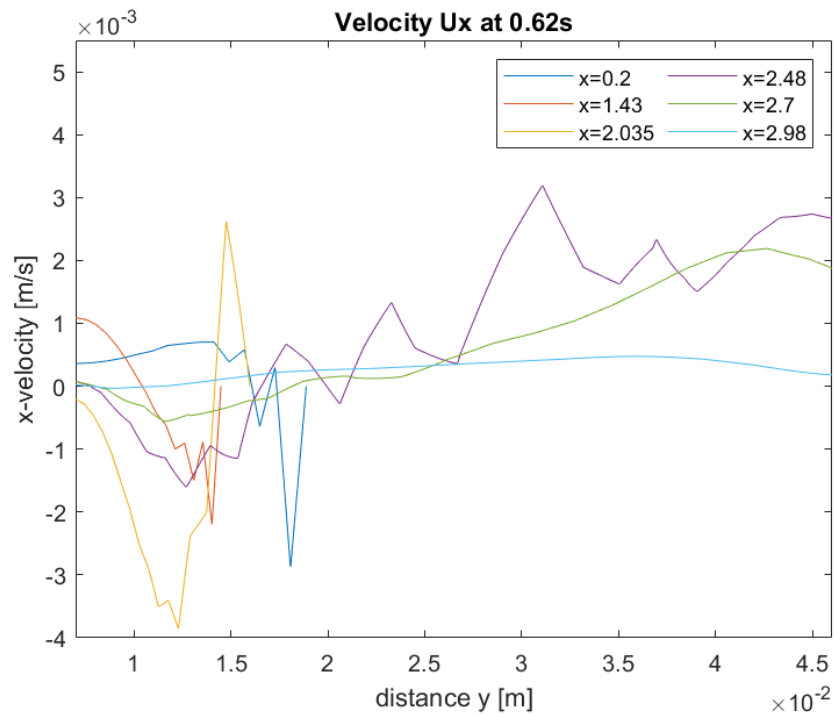


Figure 33: X-axis velocity at 0.62 s.

Figure 34 displays the coloured map, providing a visual representation of the phenomena described.

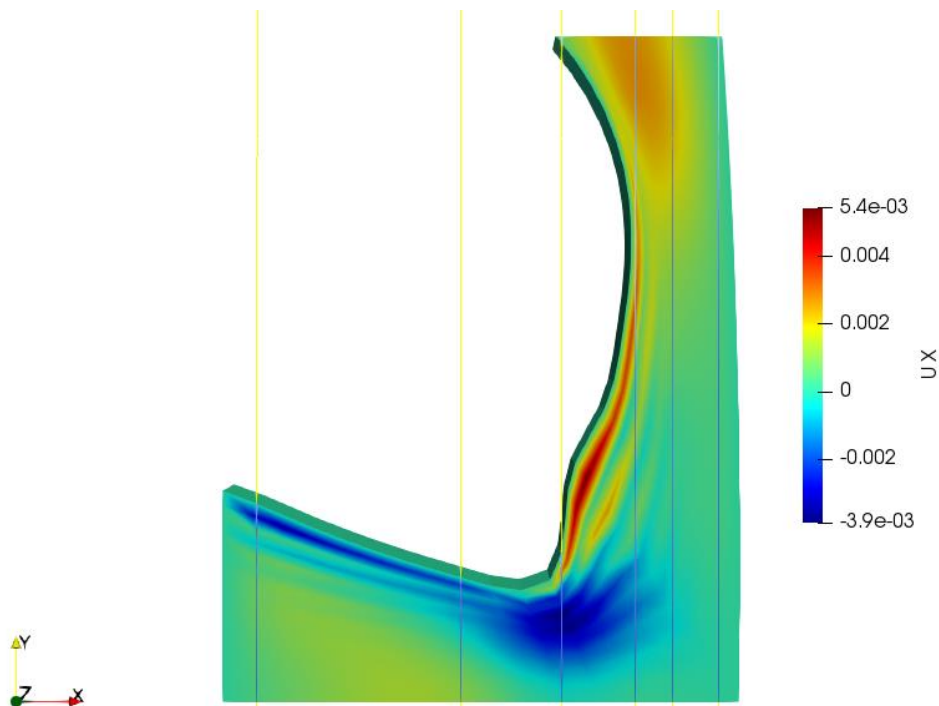


Figure 34: Coloured map of x-axis velocity at 0.62 s.

At 0.74 s, the bone is moving downwards again. In Figure 35, higher velocities are observed at the cavity's bottom, particularly just below the femur medial condyle. In the lateral cavity, the fluid motion slightly reduces the velocity, at $x=2.48$ cm and $x=2.7$ cm until a change in motion direction occurs.

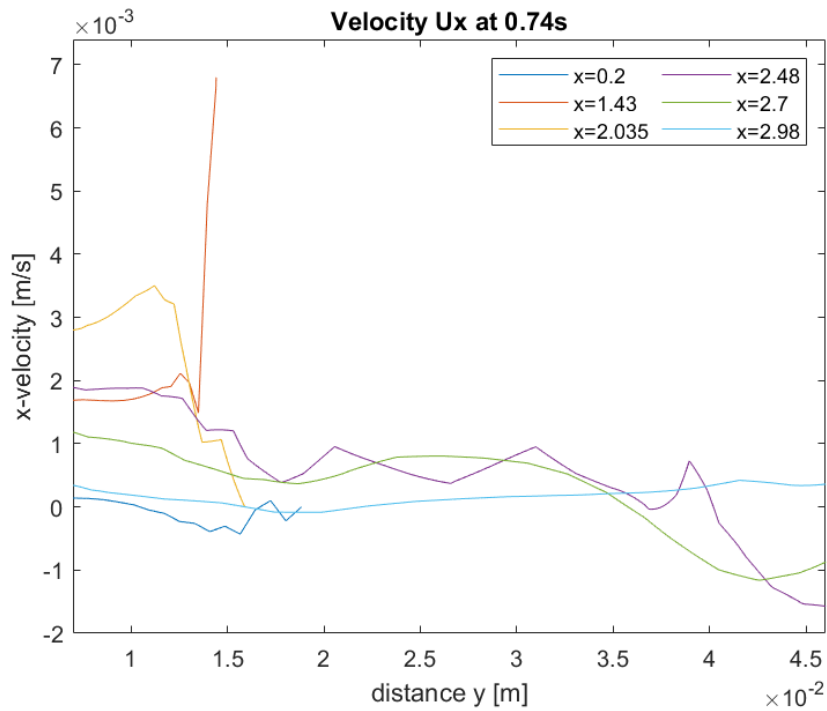


Figure 35: X-axis velocity at 0.74 s.

Figure 36 shows the coloured map for the horizontal component of velocity at 0.74 s.

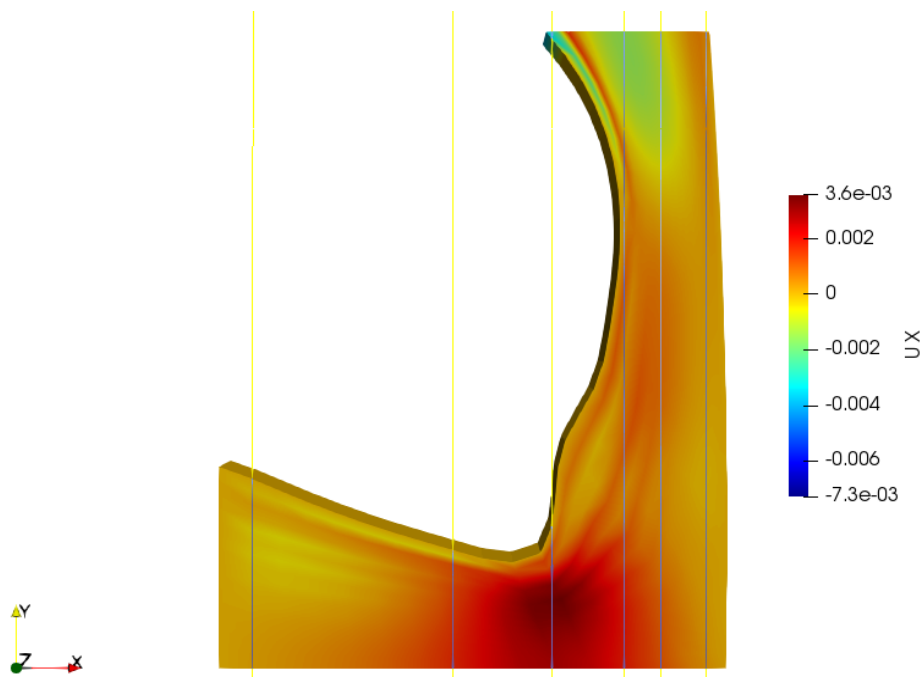


Figure 36: Coloured map of x-axis velocity at 0.74 s.

Finally, at 0.90 s the gait cycle is about to end. A change in the flow motion direction can be observed, where at the bottom of the cavity, the fluid is moving towards the left boundary, but as it gets closer to the movingWall boundary, it changes direction towards the right as in the lateral side (Figure 37).

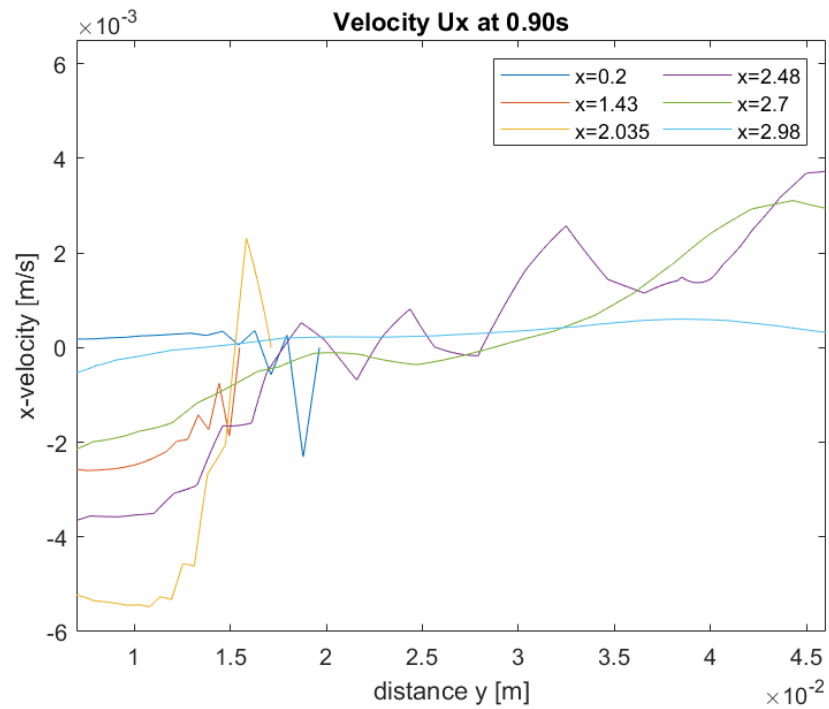


Figure 37: X-axis velocity at 0.90 s.

The highest negative velocities are observed to be in the bottom side of the cavity whereas the highest positives are in the top and in the movingWall boundary, close to the medial epicondyle (Figure 38).

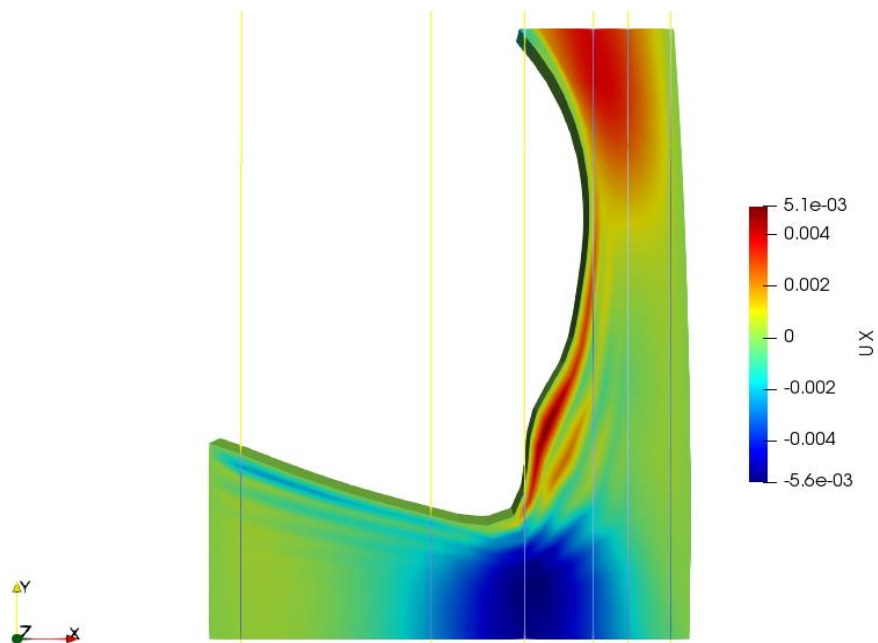


Figure 38: Coloured map of x-axis velocity at 0.90 s.

Generally, it is apparent that there is significant fluid motion in the x-direction at the bottom of the synovial cavity, resulting from the compression of the cavity, due to the approach of the femur and tibia, and the rapid expulsion of fluid towards the lateral cavity. Conversely, in the lateral cavity, the fluid motion in the x-direction is less prominent, as the fluid tends to follow the geometry of the cavity and exhibit greater movement in the y-direction.

5.3.3. Y-direction Velocity (U_y)

In this section, we will present the findings regarding the y-direction component of velocity. This component represents the vertical movement of the synovial fluid. The velocity, U_y , has been analysed at same five time steps as before. Given the significant variations in velocities, the scale of the coloured maps has been adjusted at each time step to provide a clearer visual representation of the data.

At 0.36 s, the femur initiates a vertical movement, approaching the tibia and leading to the compression of the cavity. Near the movingWall boundary, fluid velocity in y-direction reach up to -15 mm/s in the case of $x=2.035$ cm and $x=1.43$ cm. For $x=2.48$ cm, the fluid gains velocity just below the medial epicondyle whereas in the lateral side a velocity around -9 mm/s is achieved (Figure 39).

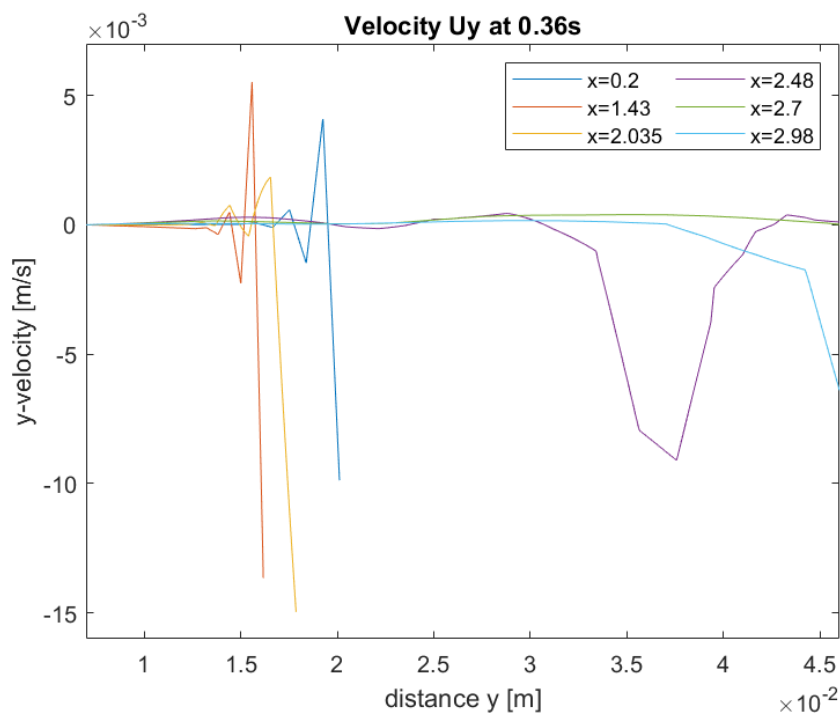


Figure 39: Y-axis velocity at 0.36 s.

At 0.36 s time step, the maximum negative velocities in y-direction are found in the movingWall, and in the upper part of the right boundary (Figure 40).

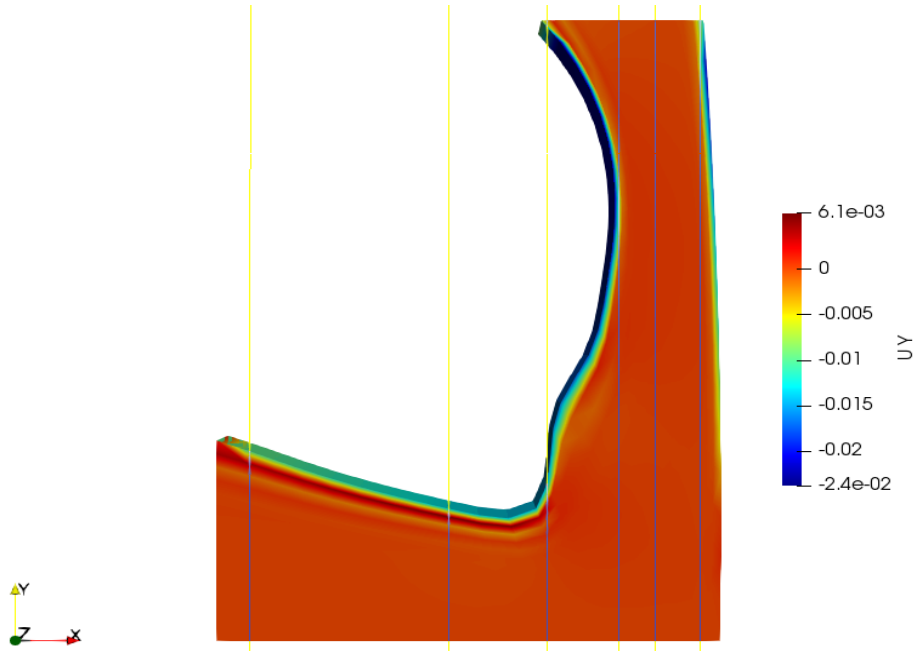


Figure 40: Coloured map of y-axis velocity at 0.36 s.

The maximum compression of the cavity, at 0.53 s, in the bottom part, near the movingWall an increase in U_y velocity is observed, reaching values around 6 mm/s. In the middle of the lateral cavity, the fluid moves upwards, forming a parabolic shape in the velocity profile and reaching a positive velocity of more than 20 mm/s (Figure 41).

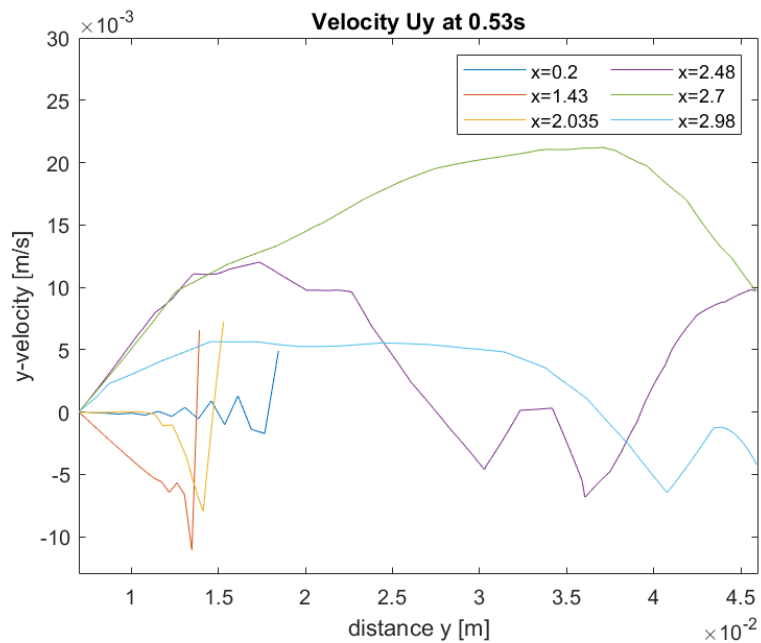


Figure 41: Y-axis velocity at 0.53 s.

The coloured map, in Figure 42, highlights the highest positive velocities within the lateral cavity, as the compression expels the fluid from the bottom and propels it towards the farFieldWall boundary.

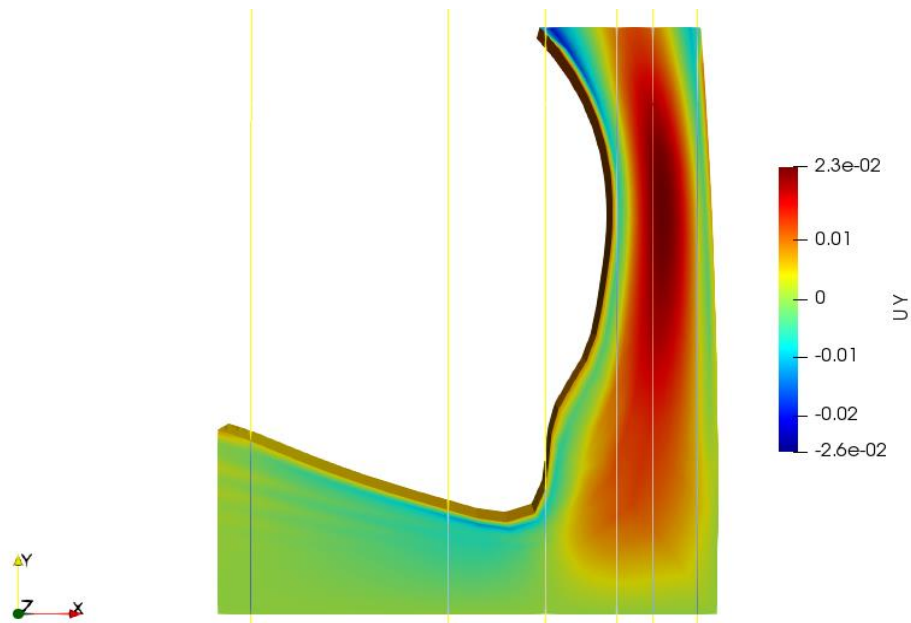


Figure 42: Coloured map of y-axis velocity at 0.53 s.

At 0.62 s, the cavity is being expanded and moving upwards. Consequently, the fluid on the upper side is propelled upwards, pushed by the bone, while the fluid on the bottom side of the lateral cavity moves towards the lower part in response to the cavity expansion (Figure 43).

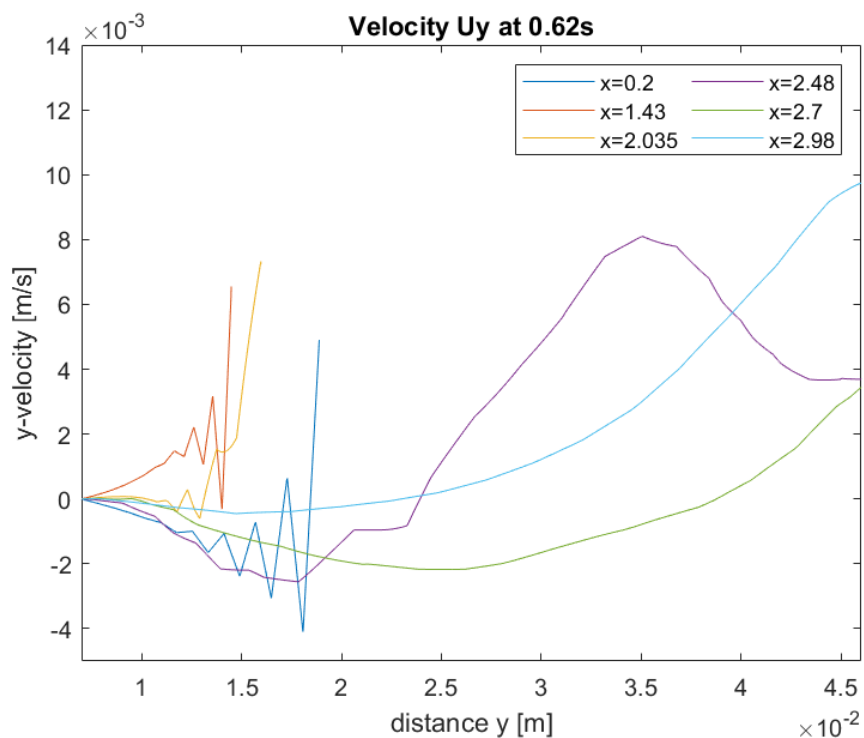


Figure 43: Y-axis velocity at 0.62 s.

The coloured map in Figure 44 shows a visual representation of these phenomena described above.

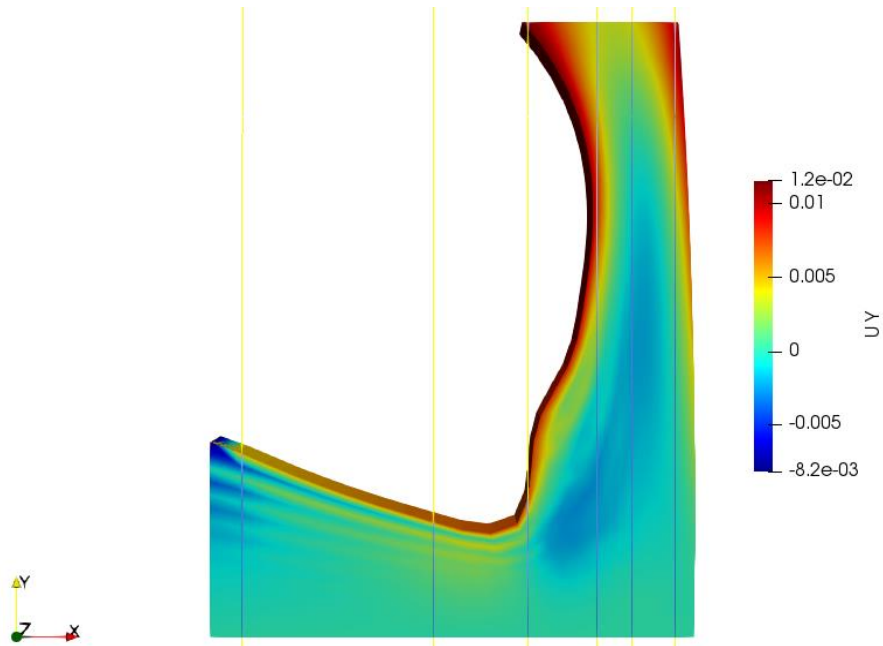


Figure 44: Coloured map of y-axis velocity at 0.62 s.

At 0.74 s, the second compression of the cavity occurs. The highest vertical velocities are located near the movingWall in the bottom side and in the middle of the lateral cavity, because of the fluid being expelled due to the compression (Figure 45), similar to previously described behaviours.

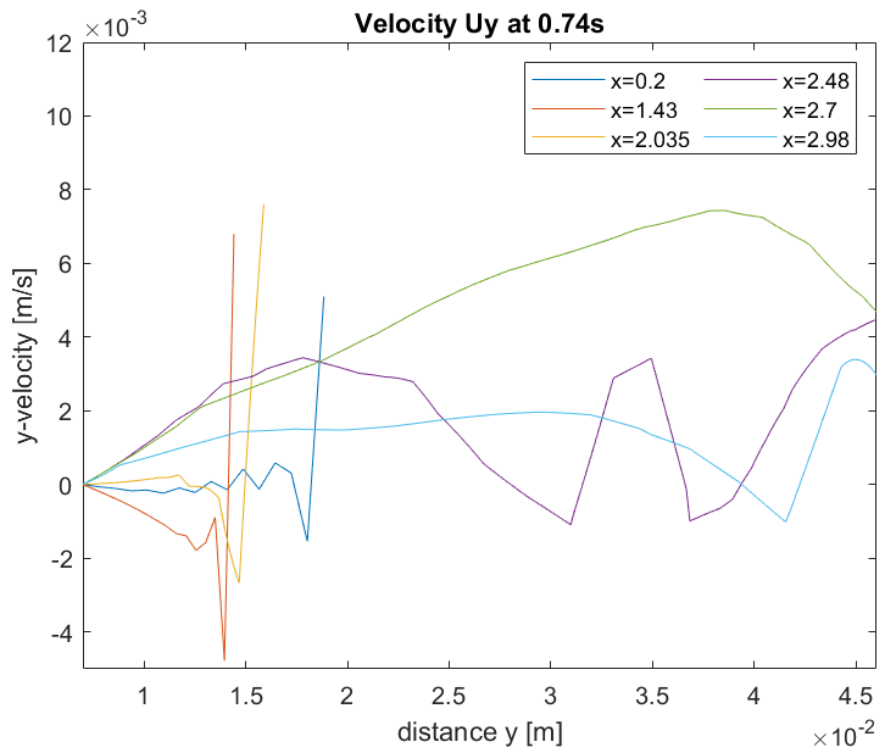


Figure 45: Y-axis velocity at 0.74 s.

Following, the coloured map for the vertical component of velocity can be seen in Figure 46.

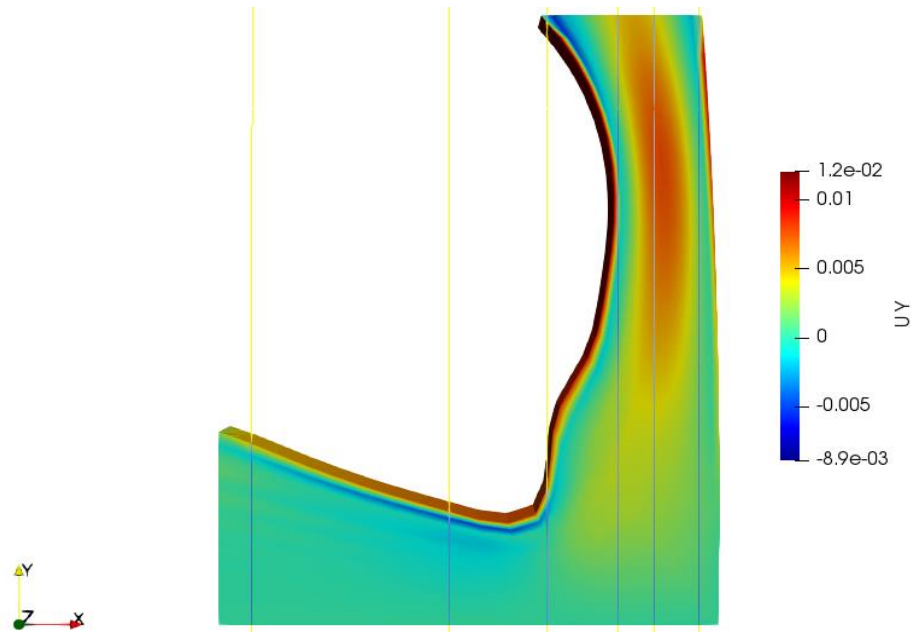


Figure 46: Coloured map of y-axis velocity at 0.74 s.

At 0.90 s, the gait cycle is becoming to an end. As the cavity expands during this time step, a behaviour similar to that observed at 0.62 s is seen. However, since this last compression is less pronounced, the value of the vertical velocities as the cavity expands is also lower (Figure 47).

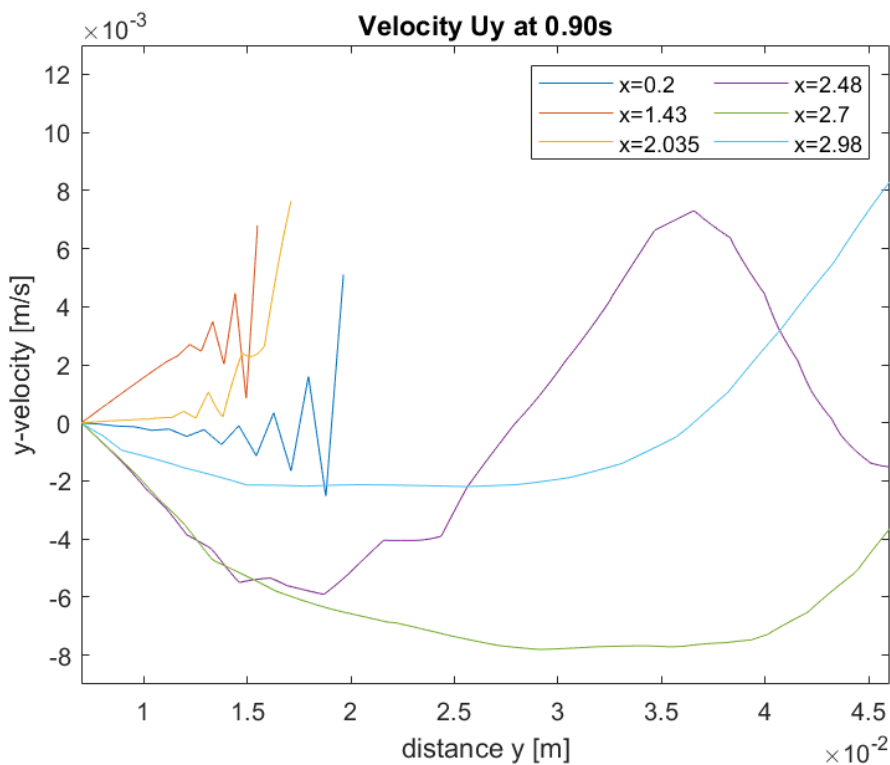


Figure 47: Y-axis velocity at 0.90 s.

As the cavity expands at 0.90s, the lateral side exhibits maximum negative velocities, indicating downward fluid motion as a response to the expansion of the bottom side of the cavity while in close proximity to the left side of the movingWall boundary, the fluid is pushed upwards by the movement of the femur (Figure 48).

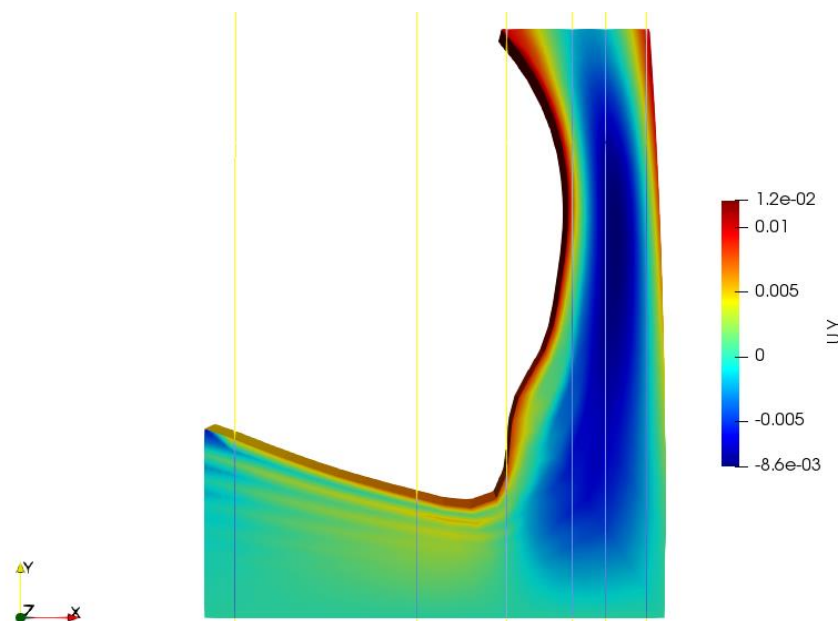


Figure 48: Coloured map of y-axis velocity at 0.90 s.

In general, as the movement of the bone has been simplified to be only vertical the fluid motion in the bottom side of the cavity consistently follows this vertical motion. This is evident in the vertical movement observed for $x=0.2$ cm, $x=1.43$ cm, and $x=2.035$ cm, as these lines are located in the bottom region of the cavity. The fluid is pushed downwards and consequently, the fluid in the bottom is also pushing upwards, as the fixedWall boundary prevents the fluid from penetrating. In the lateral cavity, significant velocity values are observed when the femur approaches the tibia, resulting in compression of the cavity and propulsion of the fluid towards the lateral cavity. The fluid follows the geometry of the cavity towards the farFieldWall boundary. Notably, some velocity profiles in the middle of the lateral cavity exhibit a parabolic shape.

5.3.4. Velocity Profile

Further analysis will be conducted on the velocity profile along the line at $x=2.7$ cm, focusing on the magnitude of velocity. This will provide valuable insights into how the fluid motion varies in response to the movement of the femur.

In Figure 49, the velocity profile between 0.63 s and 0.69 s is displayed. During this time range, there is a change in the direction of the bone's movement. From 0.63 s to 0.66 s, the bone moves downward with an approximate velocity of 11.75 mm/s. The fluid motion during this period can be described differently for the upper and lower parts of the lateral cavity. In the upper part, there is a backward movement of the fluid, while in the lower part, the fluid moves forward in response to the contraction of the bottom of the cavity and the expulsion of fluid. These time steps are represented by the continuous lines in the graph.

From 0.66 s onwards, the bone undergoes an upward movement with an approximate velocity of 7.4 mm/s, indicating separation from the tibia in accordance with the gait cycle. As the bone changes its direction of motion, there is a corresponding change in the fluid motion. This behaviour can be observed in the discontinuous lines in Figure 49, particularly at 0.67 s, where the change in direction becomes noticeable. By 0.68 s, the change in direction is complete, and the fluid now moves backward in the bottom of the lateral cavity due to the expansion of the bottom cavity and the accommodation of more fluid within it. Simultaneously, in the upper side of the lateral cavity, the fluid moves forward, reaching a maximum velocity of approximately 6.3 mm/s at around 0.69 s.

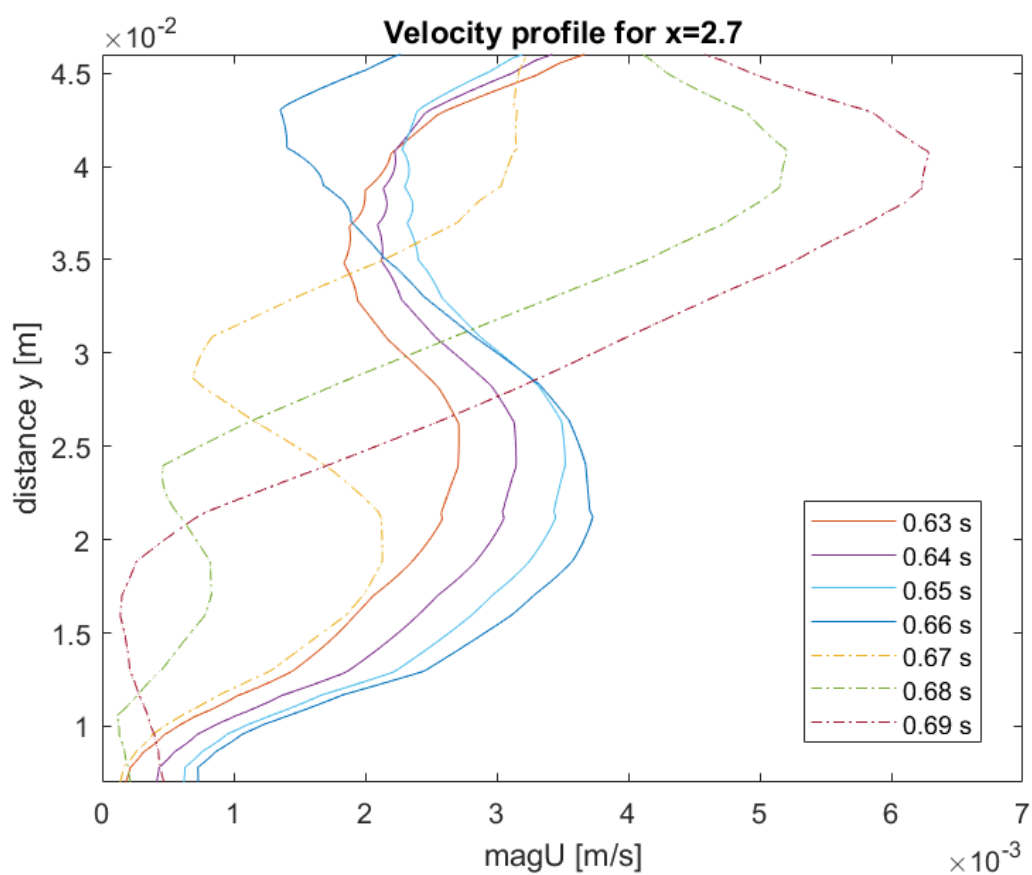


Figure 49: Velocity profile for $x=2.7$ cm at different time steps.

5.3.5. Velocity Glyphs

This sub-chapter presents velocity glyphs for the magnitude of velocity, showcasing the flow patterns and changes in the fluid motion direction over time. The glyphs are provided for some time steps ranging from 0.36 s to 0.55 s, offering a visual understanding of the evolving flow patterns.

At 0.36 s, the downward movement of the femur initiates, the fluid starts to follow this motion along the boundaries of the cavity particularly on the upper part of the MovingWall and right boundaries (Figure 50). In the next time step, 0.37 s, this downward movement continues, and the fluid in the middle of the lateral cavity is also being pushed downwards (Figure 51).

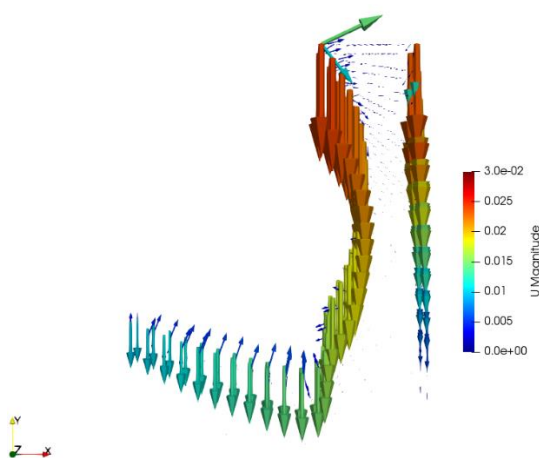


Figure 50: Velocity glyphs at 0.36 s.

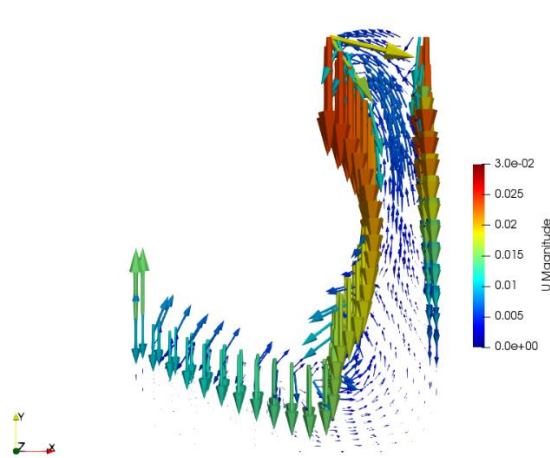


Figure 51: Velocity glyphs at 0.37 s.

At 0.38 s, due to the downward movement of the bone, the bottom of the cavity experiences compression, leading to the expulsion of fluid towards the lateral side of the cavity (Figure 52). In the following time step, at 0.39 s, the fluid has gained some velocity (Figure 53).

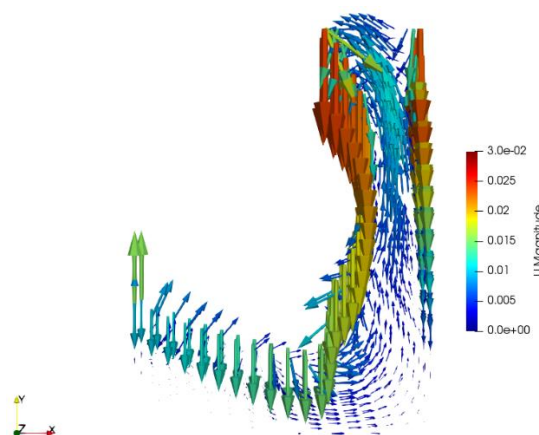


Figure 52: Velocity glyphs at 0.38 s.

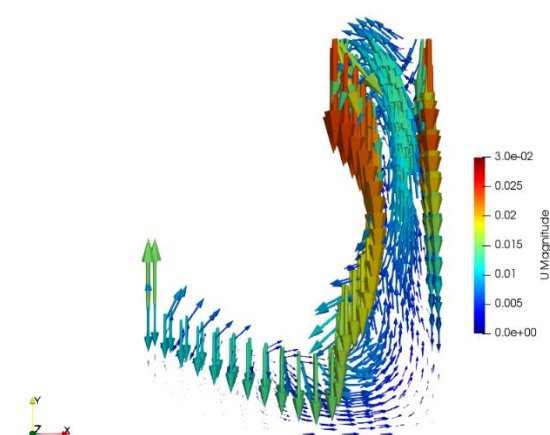


Figure 53: Velocity glyphs at 0.39 s.

The compression of the cavity continues until 0.53 s. The fluid in the lateral side of the cavity can be seen gaining velocity, indicating the ongoing motion resulting from the compression (Figure 54). At 0.52 s, higher velocities of the fluid in the bottom of the cavity are found, specifically between the medial condyle and epicondyle (Figure 55).

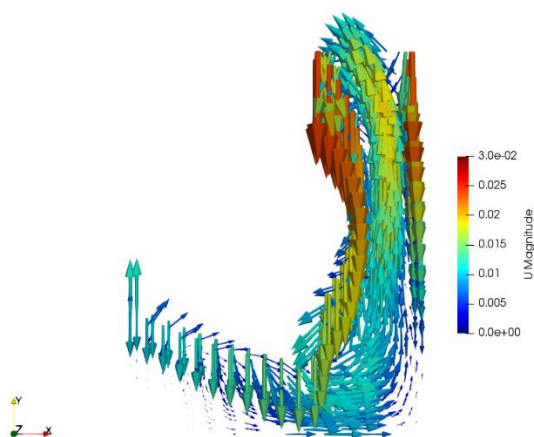


Figure 54: Velocity glyphs at 0.45 s.

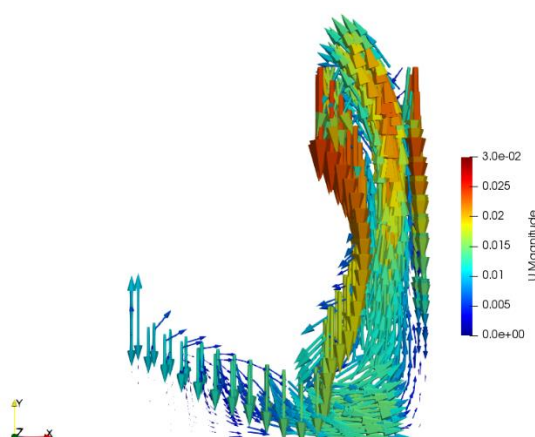


Figure 55: Velocity glyphs at 0.52 s.

Velocity glyphs at 0.52 s will be further analysed. This time step corresponds to nearly maximum compression of the cavity. High positive velocities in x-direction are observed in the bottom of the cavity, indicating horizontal movement of the fluid towards the lateral cavity (Figure 56). On the upper side, negative velocities are observed, suggesting that the fluid encounters the farFieldWall boundary and moves towards the left side (movingWall boundary). In the case of y-direction velocity, the maximum positive velocities are found in the lateral side of the cavity, as the fluid expelled from the bottom of the cavity follows the cavity's geometry, resulting in movement towards the upper boundary (farFieldWall boundary) (Figure 57).

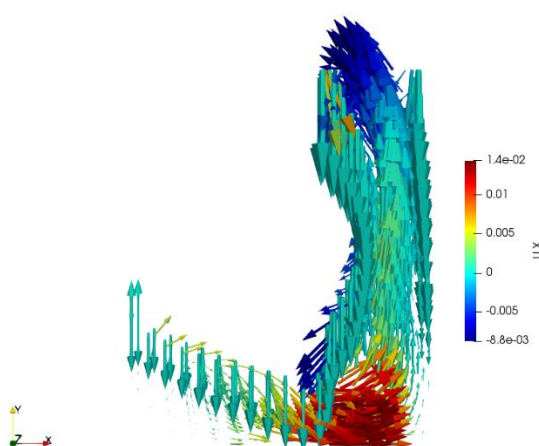


Figure 56: X-direction velocity glyphs at 0.52 s.

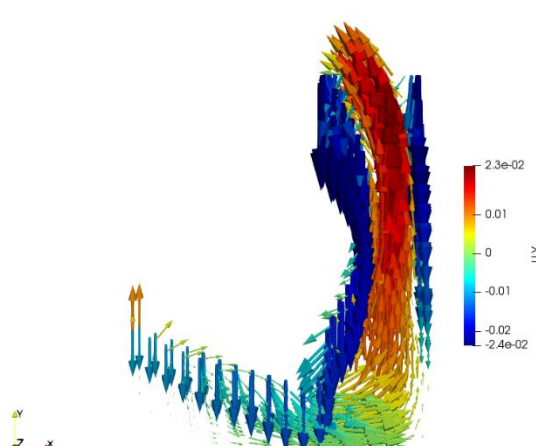


Figure 57: Y-direction velocity glyphs at 0.52 s.

Following with the glyphs depicting the magnitude velocity at 0.53 s, when the motion of the femur changes direction with an approximate velocity of 24 mm/s, moving upwards (Figure 58). As the fluid expelled from the bottom of the cavity was accumulated on the upper side of the movingWall boundary this change in motion results in high velocity within that region. On the bottom side of the movingWall, the upward motion imposed by the bone can be observed. At 0.54 s, the cavity is being expanded and the fluid will be once again redistributed along the bottom side (Figure 59).

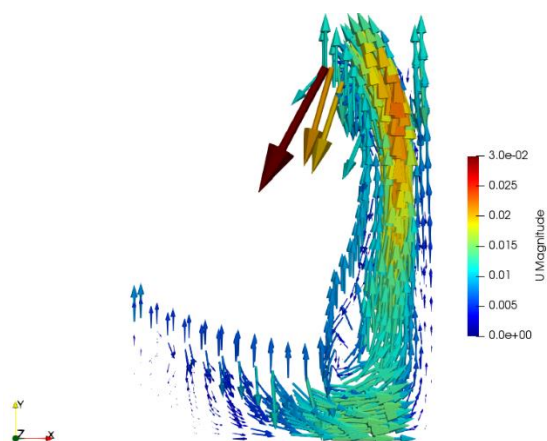


Figure 58: Velocity glyphs at 0.53 s.

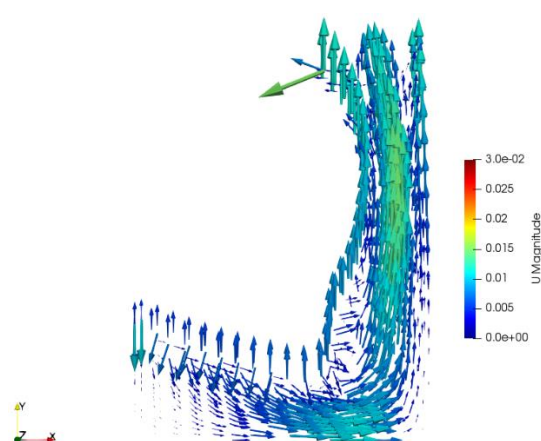


Figure 59: Velocity glyphs at 0.54 s.

At 0.55 s, the upward motion of the bone continues as it separates from the tibia in accordance with the gait cycle. The velocity of the fluid decreases due to the expansion of the bottom of the cavity and accommodation of the same along the bottom part. The highest velocities for this time step can be observed close to the upper side of the movingWall and the right boundaries, as the movement of the bone pushes the surrounding fluid to follow a similar motion (Figure 60).

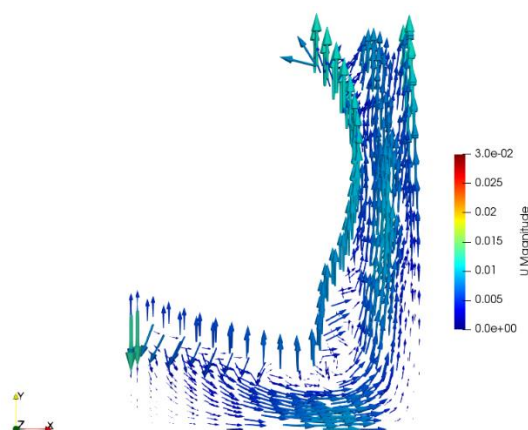


Figure 60: Velocity glyphs at 0.55 s.

5.4. Surface Flow

Since the study is dealing with a closed cavity, the validation of the simulation will involve calculating the Surface Flow using the post-processing tool ParaView. In an accurate simulation, the expected value for all boundaries should be zero, as the idea is to maintain the fluid inside the synovial cavity, mirroring the behaviour observed in reality in the synovial cavity. By setting the expected value for all boundaries to zero, describing them as walls, a constraint that the fluid should not leave the cavity is imposed. This is a reasonable assumption for a closed cavity, such as a synovial cavity, where the fluid is contained within the boundaries.

The Surface Flow filter in ParaView will be used to check it. This filter is used to visualize and analyse the flow of a vector field on a surface. It is particularly useful for visualizing fluid flow or other vector fields that are constrained to a surface, such as velocity fields on the surface of an object. When you apply the Surface Flow filter to your data, it takes a vector field dataset as input and projects the vectors onto the surface geometry. This creates streamlines or ribbons that represent the flow direction and magnitude on the surface.

The Surface Flow will be computed for each boundary. The filter Extract Block is used to extract the patches of study. In Figure 61, an example of the filter used on the movingWall boundary can be seen.

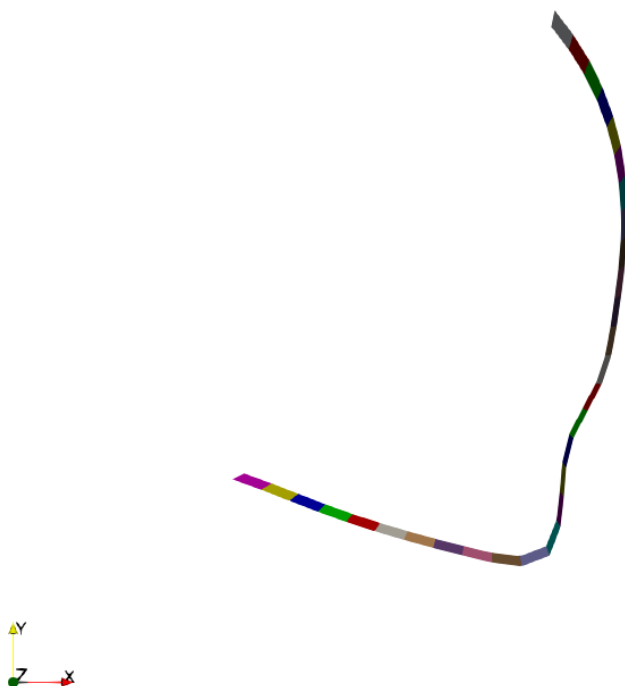
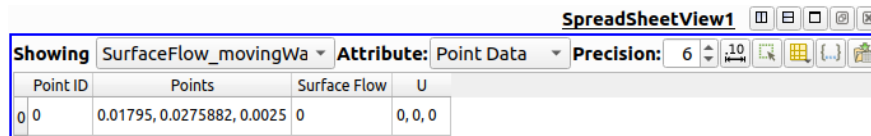


Figure 61: Extract Block filter in movingWall boundary in ParaView.

Following, the Surface Flow filter is selected, and U (velocity) is chosen as the input vector. Finally, the user can obtain the value for the surface flow in different points of the surface (Figure 62).



The screenshot shows the 'SpreadSheetView1' window in ParaView. The window title is 'SpreadSheetView1'. Below the title bar, there are several controls: 'Showing' set to 'SurfaceFlow_movingWa', 'Attribute' set to 'Point Data', and 'Precision' set to '6'. The main area of the window contains a table with the following data:

Point ID	Points	Surface Flow	U
0	0	0.01795, 0.0275882, 0.0025	0
			0, 0, 0

Figure 62: Capture of surface flow in ParaView.

By applying the "Surface Flow" filter in ParaView, the flow on the surface of the cavity is visualized and it is possible to assess if the calculated flow aligns with the expected behaviour. If the flow vectors or streamlines indicate any fluid movement out of the cavity, it would suggest an issue with the simulation or the boundary conditions. In the case of study, this validation step has confirmed that the surface flow has a value of zero for all boundaries, as anticipated.

6. Environmental analysis

The environmental impact of the project is minimal because it was conducted using a personal electronic device, to be exact an HP ENVY 16inch. The manufacturing process, distribution, use and end of life have been the only environmental impact. To be able to calculate it, data obtained from the manufacturer, HP, will be considered. The information provided here represents the lifecycle carbon footprint of an industry-average notebook computer with the specifications listed in Assumptions table [32], Table 3

According to Figure 63, the manufacturing phase contributes 70% to the overall carbon footprint. This phase includes the production of various components such as the motherboard, SSD, and display, which are responsible for a significant portion of the emissions, as indicated in Table 2. The use phase accounts for 23% of the emissions, while the distribution phase only contributes 7% of the greenhouse gas emissions.

Table 2: Manufacturing GHG Emissions of an HP Envy 16inch Laptop.

Manufacturing Breakout

Mainboard and other boards	38.1%
Solid State Drive (SSD)	28.0%
Display	16.7%
Chassis	5.2%
Power Supply Unit & External Cables	4.5%
Batteries	3.7%
Others*	3.2%
Packaging	0.6%

to provide the most accurate environmental impact results, but uncertainty will never be completely minimized and results should be considered accordingly [32].

The estimated impact considering these assumptions presented in Table 3, was of 290 kg CO₂eq for 4 years of service life. The current project was made in 4 months, so based on the proportional calculation, the total carbon footprint of the project is estimated to be 24,17 kg CO₂eq.

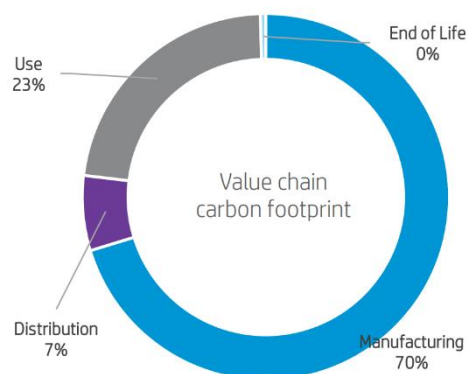


Figure 63: Greenhouse gas emissions (GHG) of an HP Envy 16inch laptop.

HP's environmental impact calculations are done in accordance with ISO 14040/44. All estimates of impact results are uncertain, resulting largely from data limitations and data quality [32]. To mitigate this uncertainty, HP has developed HP-specific tools that use a combination of HP processes and product data, as well as high-quality lifecycle assessment data [32]. HP strives

Table 3: Assumptions made to calculate of the GHG emissions.

Assumptions	
Lifetime of product (years)	4
Use location	North America
Use energy demand (kWh/year)	30.63
Product weight (kg)	2.6
Screen size (in)	16"
Final manufacturing location	China

7. Conclusions

The utilization of OpenFOAM, an open-source software, facilitated the achievement of a stable simulation through the application of suitable meshing techniques and the provision of a well-defined problem description with appropriate boundary conditions. The simulation was focused on modelling an incompressible Newtonian fluid, the synovial fluid, inside the synovial cavity which was achieved with minimal computational costs while ensuring control over the Courant number. By incorporating realistic parameters and accurately designing the cavity geometry, significant findings could be extracted and thoroughly analysed.

The study demonstrated that a higher fluid viscosity resulted in increased resistance to flow, leading to elevated pressure within the system. This phenomenon was attributed to reduced molecular mobility and increased internal friction caused by higher fluid viscosity, which restricts the free volume and impacts the fluid's ability to flow freely.

Additionally, the simulation revealed dynamic changes in the mesh geometry during the compression and expansion of the cavity, resulting in a reduction of total volume. When moving boundaries are included in the model, the dynamic mesh can change its geometry during the simulation. This behaviour was particularly observed in the compression of the mesh, leading to a reduction of total volume, which is later recovered during the expansion of the cavity.

By incorporating realistic parameters, the study captured the fluid dynamics and highlighted the redistribution of fluid within a closed cavity during the gait cycle. When the synovial cavity gets compressed, the fluid must be redistributed to accommodate the reduced space, resulting in a significant increase in pressure. In terms of velocity motion, after compression in the bottom of the cavity, the fluid is expelled towards the lateral side. The fluid then follows the geometry of the cavity, moving laterally towards the upper boundaries.

Furthermore, during the simulation it has been observed that due to the cavity's geometry, the velocity patterns in the bottom, when the femur approaches the tibia and compression occurs, the x-direction velocity has a more significant value as the synovial fluid moves horizontally towards the lateral side. In contrast, in the lateral side of the cavity, the y-direction velocity played a more prominent role. It exhibited predominantly vertical motion in both upward and downward directions, with less horizontal motion observed.

These findings, obtained through the use of a robust simulation framework with a short computation time and the inclusion of realistic parameters, greatly contribute to understanding the synovial fluid behaviour within the knee's synovial cavity.

The study represents a continuation of an ambitious project with the objective of creating a virtualization of the knee. Improving the geometry, parameter simulation, and the implementation of appropriate boundary conditions was a significant step towards achieving this goal. For future research, the menisci should be considered and added to the model. Creating an even more realistic cavity by making it thinner on the lateral side could enhance the accuracy of the virtualization. However, such a modification may introduce computational risks, as the Courant number could increase significantly. Additionally, conducting a more detailed study on the pressure and forces exerted by the bone on the synovial fluid would provide valuable insights and further the understanding of the knee's biomechanics. Finally, to provide a more realistic representation, introducing a more accurate gait cycle motion into the model is advisable as the current approximation allowed for the analysis of fluid behaviour but could be further refined to enhance realism.

Economic analysis

This section refers to the project's development costs. The development costs for the project primarily include personal costs (hours invested by the engineers) and software costs. The personal costs are further broken down based on the hours invested by each engineer.

Three engineers were involved in this project, the accounted hours are counting for 4 months that we have been working on the project, although this would be only for this specific study as the global project has been ongoing for longer.

Two of the engineers, the supervisor, and the co-supervisor, invested their time in weekly meetings. The specific hours invested by the student are shown in Table 4: Labor costs. It is stated that 20% of the student's time was dedicated to familiarizing themselves with the software used for modelling the problem, 60% was spent directly on developing the model and extracting results, and 20% was allocated for working on the final report.

Table 4: Labor costs.

	Hours Worked	Cost per hour worked [€/hour]	Final Cost [€]
Engineer 1 (director)	30	30	900
Engineer 2 (co-director)	30	30	900
Engineer 3 (student)	750	30	22,500
		TOTAL	24,300€

Regarding software costs, in Table 5, four different software packages have been used. Two of them, SALOME and OpenFOAM, are open-source and available for free. However, licenses are required for the other two software packages, Microsoft Word, and MATLAB.

Table 5: Software costs.

	License Cost [€]	Time of use [month]	Time of active license [month]	Final Cost [€]
SALOME	0	4	-	0
OpenFOAM	0	4	-	0
Microsoft 365	69	4	12	23
MATLAB	69	4	12	23
			TOTAL	46€

So that, the total cost of the project, including the labour and software costs, is 24.346,00 €.

References

- [1] A. Seth *et al.*, “OpenSim: Simulating musculoskeletal dynamics and neuromuscular control to study human and animal movement,” 2018.
- [2] G. Chen, Q. Xiong, P. J. Morris, E. G. Paterson, A. Sergeev, and Y.-C. Wang, “OpenFOAM for Computational Fluid Dynamics,” *Notices of the American Mathematical Society*, vol. 61, no. 4, p. 354, Apr. 2014, doi: 10.1090/noti1095.
- [3] P. Pustejovská, “Mathematical Modeling of Synovial Fluids Flow,” 2008.
- [4] M. Alshehri, “Computational Model for the Generalised Dispersion of Synovial Fluid,” *International Journal of Advanced Computer Science and Applications*, vol. 8, Jun. 2017, doi: 10.14569/IJACSA.2017.080218.
- [5] M. Blewis, G. Nugent-Derfus, T. Schmidt, B. Schumacher, and R. Sah, “A model of synovial fluid lubricant composition in normal and injured,” *Eur Cell Mater*, vol. 13, pp. 26–39, Jun. 2007, doi: 10.22203/eCM.v013a03.
- [6] K. Pekkan, R. Nalim, and H. Yokota, “Computed Synovial Fluid Flow in a Simple Knee Joint Model,” in *Proceedings of the ASME/JSME Joint Fluids Engineering Conference*, Jun. 2003. doi: 10.1115/FEDSM2003-45430.
- [7] L. A. and G.-G. S. R. and A.-C. A. and V.-G. G. Martínez-Gutiérrez N. and Ibarra-Bracamontes, “Numerical Modeling of the Knee Synovial Joint Under Deformation Using the Finite Volume Method,” in *Recent Advances in Fluid Dynamics with Environmental Applications*, L. D. G. and M. A. and L. A. and R.-C. G. Klapp Jaime and Sigalotti, Ed., Cham: Springer International Publishing, 2016, pp. 419–433.
- [8] J. Hron, J. Málek, P. Pustějovská, and K. Rajagopal, “On the Modeling of the Synovial Fluid,” *Advances in Tribology*, vol. 2010, Jun. 2010, doi: 10.1155/2010/104957.
- [9] A. Leiva, “MODELITZACIÓ COMPUTACIONAL DE LA CAVITAT SINOVIAL DEL GENOLL,” Polytecnic University of Catalonia, 2021.
- [10] A. J. Villegas, “VIRTUAL MODELLING OF MUSCULOSKELETAL SOFT TISSUE: APPLICATIONS TO KNEE MENISCI,” Polytecnic University of Catalonia, Barcelona, 2021.
- [11] Medi GmbH, “The knee: Anatomy and function,” <https://www.medi.de/en/diagnosis-treatment/knee-pain/anatomy-knee/>.

- [12] D. M. Daniels, "Knee Ligaments: Structure, Function, Injury and Repair," *Raven Press*, vol. New York, 1990.
- [13] M. Kazemi, Y. Dabiti, and L. P. Li, "Recent Advances in Computational Mechanics of the Human Knee Joint," *Computational and Math Methods in Medicine*, 2013.
- [14] J. K. Loudon, "BIOMECHANICS AND PATHOMECHANICS OF THE PATELLOFEMORAL JOINT," *Int J Sports Phys Ther.*, 2016.
- [15] S. Affatato, "Biomechanics of the knee," *Surgical Techniques in Total Knee Arthroplasty (TKA) and Alternative Procedures*, pp. 17–35, Jan. 2015, doi: 10.1533/9781782420385.1.17.
- [16] A. Pourcho, "Soft Tissue of the Knee Joint," *SPORTS-health*, 2015.
- [17] V. C. Scanlon and T. Sanders, "The Skeletal System," in *Essentials of Anatomy and Physiology*, 1996.
- [18] P. J. Mansfield and D. A. Neumann, "Structure and Function of Joints," in *Essentials of Kinesiology for the Physical Therapist Assistant*, Third.2019.
- [19] E. Maniaki, "Risk factors, activity monitoring and quality of life assessment in cats with early degenerative joint disease," 2020. doi: 10.13140/RG.2.2.34754.71366.
- [20] S. M. Zindge and J. Slamin, "Biomechanics of the knee joint, as they relate to arthroplasty," in *Orthopaedics and Trauma* , 2016.
- [21] S. D. Masouros, A. M. J. Bull, and A. A. Amis, "(i) Biomechanics of the knee joint," *Orthop Trauma*, vol. 24, no. 2, pp. 84–91, Apr. 2010, doi: 10.1016/J.MPORTH.2010.03.005.
- [22] S. Fathy and M. Elmessiry, "Study of the Effect of Cyclic Stress on the Mechanical Properties of Braided Anterior Cruciate Ligament (ACL)," *J Text Sci Eng*, vol. 06, Jun. 2016, doi: 10.4172/2165-8064.1000252.
- [23] L. Hampton and K. Jackson, "Synovium and Synovial Fluid," *Physopedia*.
- [24] S. Tarafder and C. H. Lee, "Synovial Joint: In Situ Regeneration of Osteochondral and Fibrocartilaginous Tissues by Homing of Endogenous Cells," *In Situ Tissue Regeneration: Host Cell Recruitment and Biomaterial Design*, pp. 253–273, Jan. 2016, doi: 10.1016/B978-0-12-802225-2.00014-3.

- [25] E. Radin, I. Paul, D. Swann, and E. Schottstaedt, "Lubrication of synovial membrane," *Ann Rheum Dis*, vol. 30, pp. 322–325, Jun. 1971, doi: 10.1136/ard.30.3.322.
- [26] A. F. Depalma, *Diseases of the Knee: Management in Medicine and Surgery*, 1st ed. Philadelphia, PA, USA: .B. Lippincott Company, 1954.
- [27] A. J. Freemont and E. Abdellatif, "Synovial fluid analysis," *Rheumatology: Sixth Edition*, vol. 1–2, pp. 237–241, 2015, doi: 10.1016/B978-0-323-09138-1.00031-0.
- [28] K. Wierzcholski, "Topology of calculating pressure and friction coefficients for time-dependent human hip joint lubrication," 2011.
- [29] "Salome Platform Documentation," *Version: 9.10.0. 2003-2007 OPEN CASCADE, EADS/CCR, LIP6, CEA/DEN, CEDRAT, EDF R&D, LEG, PRINCIPIA R&D, BUREAU VERITAS*.
- [30] "Medial Condyle," *Earth's Lab*, 2019.
- [31] NSW Ministry of Health, "MRI Knee," *Medical Imaging*, Feb. 24, 2015.
- [32] "OpenFoam User Guide, 4.2 Boundaries, 4.2.1 Specification of patch types in OpenFOAM," *OpenCFD Ltd*, 2023.
- [33] V. Abella, "How are dimension units on openFoam?" [Online]. Available: <https://scicomp.stackexchange.com/q/30122>
- [34] D. Wang, K.-M. Lee, and J. Ji, "A Passive Gait-Based Weight-Support Lower Extremity Exoskeleton With Compliant Joints," *IEEE Transactions on Robotics*, vol. 32, pp. 1–11, Jun. 2016, doi: 10.1109/TRO.2016.2572692.
- [35] P. Malcolm, W. Derave, S. Galle, and D. Clercq, "A Simple Exoskeleton That Assists Plantarflexion Can Reduce the Metabolic Cost of Human Walking," *PLoS One*, vol. 8, p. e56137, Jun. 2013, doi: 10.1371/journal.pone.0056137.
- [36] K.-M. Lee and D. Wang, "Design analysis of a passive weight-support lower-extremity-exoskeleton with compliant knee-joint," *Proc IEEE Int Conf Robot Autom*, vol. 2015, pp. 5572–5577, Jun. 2015, doi: 10.1109/ICRA.2015.7139978.
- [37] J. L. Pons, *Wearable Robots: Biomechatronic Exoskeleton*. New York, NY, USA: Wiley, 2008.
- [38] Z. Lerner, D. Damiano, H.-S. Park, A. Gravunder, and T. Bulea, "A Robotic Exoskeleton for Treatment of Crouch Gait in Children With Cerebral Palsy: Design and Initial Application," *IEEE*

- Transactions on Neural Systems and Rehabilitation Engineering*, vol. 25, p. 1, Jun. 2016, doi: 10.1109/TNSRE.2016.2595501.
- [39] J. Zhu, Y. Wang, J. Jiang, B. Sun, and H. Cao, "Unidirectional variable stiffness hydraulic actuator for load-carrying knee exoskeleton," *Int J Adv Robot Syst*, vol. 14, p. 172988141668695, Jun. 2017, doi: 10.1177/1729881416686955.
- [40] G. Serrancolí, A. L. Kinney, and B. J. Fregly, "Influence of musculoskeletal model parameter values on prediction of accurate knee contact forces during walking," *Med Eng Phys*, vol. 85, pp. 35–47, Nov. 2020, doi: 10.1016/j.medengphy.2020.09.004.
- [41] C. J. Greenshields, "OpenFOAM User Guide," *The OpenFOAM Foundation*, Jul. 12, 2022.
- [42] R. Courant, K. Friedrichs, and H. Lewy, "Über die partiellen Differenzgleichungen der mathematischen Physik," *Math Ann*, vol. 100, no. 1, pp. 32–74, 1928, doi: 10.1007/BF01448839.
- [43] F. Moukalled, L. Mangani, and M. Darwish, "Fluid Mechanics and Its Applications The Finite Volume Method in Computational Fluid Dynamics." [Online]. Available: <http://www.springer.com/series/5980>
- [44] M. S. Shadloo, D. Le Touzé, and G. Oger, "Smoothed particle hydrodynamics method for fluid flows, towards industrial applications-Motivations, current state, and challenges." Jun. 2016.
- [45] "What Are the Navier-Stokes Equations?," *Numeric Backgrounds for CFD and FEA*, Feb. 13, 2023.
- [46] "OpenFoam User Guide, 6.3 Solution and algorithm control, 6.3.3 PISO and SIMPLE algorithms," *OpenCFD Ltd*, 2023.
- [47] J. H. Ferziger and M. Perić, *Computational Methods for Fluid Dynamics*, 3rd ed. Springer, 2002.
- [48] "OpenFoam User Guide, 7. Post-processing, 7.1 paraFoam," *OpenCFD Ltd*, 2023.